J. Plasma Phys. (2026), *vol*. 92, E47 doi:10.1017/S0022377826101536

Comparison of turbulent electron heat flux model predictions of the H-mode electron pedestal temperature profile across isotope mix and gas fuelling rate scans in JET with the Be/W wall

Anthony Robert Field[1], Lorenzo Frassinetti[2], Benjamin Chapman-Oplopiou[1], Colin Malcolm Roach[1], Samuli Saarelma[1], Leonard-Petru Turica[1,3,4] and JET Contributors[#]

[1]United Kingdom Atomic Energy Authority, Culham Campus, Abingdon, Oxon OX14 3DB, UK
[2]Division of Fusion Plasma Physics, KTH, Stockholm, Sweden
[3]Rudolf Peierls Centre for Theoretical Physics, University of Oxford, Oxford OX13PU, UK
[4]University College, Oxford OX1 4BH, UK

Corresponding author: Anthony Robert Field, anthony.field@ukaea.uk

(Received 2 December 2025; revision received 4 February 2026; accepted 2 March 2026)

Predictions of the pedestal temperature profile calculated using a model for electron-temperature-gradient (ETG) turbulent electron heat transport Field *et al*. (2023 *Philos. Trans. R. Soc. A*, vol. **381**, p. 20210228) are compared with the pedestal structure of H-mode plasmas in JET-Be/W (with Be wall and W divertor) over scans of the deuterium–tritium (D:T) isotope mix and hydrogenic gas fuelling rate Frassinetti *et al*. (2023 *Nucl. Fusion*, vol. **63**, p. 112009). Predictions for the electron temperature at the location of the density pedestal top $T_e(\psi_N^{n_{e,top}})$ (where ψ_N, is the normalised poloidal flux) are found to agree well with measured values over both scans across the full range of D:T ratio. However, the pedestal top temperature $T_{e,ped}$, typically located somewhat inside the density pedestal top, is under-predicted by as much as a factor $\sim$2. This implies that the ETG heat flux scaling appropriate for the steep-density gradient region, on which the model is based, is not applicable where the density gradient is weak. This difference might be attributed to a difference between the physics of the ETG turbulence in regimes where the density gradient is either strong or weak, which are thought to be dominated by either the 'slab' or 'toroidal' branches of ETG turbulence. Other branches of turbulence might also play a role in the electron heat transport, particularly in regions of weak-density gradient. As in the experiment, the predicted T_e across the pedestal decreases with the ratio of separatrix to pedestal density $n_{e,sep}/n_{e,ped}$, which increases with the gas fuelling rate. Results from three models combining the ETG heat flux model with the EPED1 pedestal (EPED) model (Snyder *et al*., *Phys. Plasmas*, 2009, vol. 16, p. 056118) are also presented, including one which also incorporates the density pedestal prediction mode of Saarelma *et al*. (*Nucl. Fusion*, 2023, vol. 63, p. 052002), this model providing a complete prediction of the pedestal profiles.

[#]See the author list of Maggi *et al*. *Nucl. Fusion*, 2024, vol. 64, p. 112012.

Key words: fusion plasma, plasma confinement, plasma instabilities

1. Introduction

In a high-confinement 'H-mode' tokamak plasma (Wagner *et al*. 1982), an edge transport barrier (a narrow region of reduced particle and heat diffusivity) forms spontaneously at the plasma periphery, resulting in much stronger gradients of density and temperature, known as the H-mode 'pedestal' just inside the last closed flux surface (LCFS) or 'separatrix'. This pedestal increases the total particle and energy content of the plasma and thereby the overall energy confinement. Hence, for predictions of the performance of future devices, it is crucial to be able to predict the electron density $n_{e,ped}$ and temperature $T_{e,ped}$ at the top of the pedestal, which provide the boundary conditions for calculation of the density and temperature profiles across the confined 'core' plasma and thereby the total stored thermal energy W_{pl} of the plasma.

Future fusion devices designed to demonstrate the conditions of a burning D–T plasma, e.g. ITER, DEMO or STEP (Ikeda 2009; Federici *et al*. 2014; Nuttall *et al*. 2020), will be run with plasmas formed from a 50 : 50 D–T mixture for thermonuclear operation, so it is important to understand the effect of the relative isotope mass, $A_{eff} = \sum (c_i A_i)/\sum c_i$, where $A_i = m_i/m_p$ (where m_i is the ion mass and m_p is the proton mass) is the mass number and $c_i = n_i/n_e$ (where n_i and n_e are the ion and electron number densities) is the concentration of each hydrogenic isotope (H, D and T)), on confinement and heat transport across the core and pedestal regions of the plasma. Hence, any model, either theory based, a reduced model or a simulation of turbulent heat transport, to be used for prediction of the pedestal temperature $T_{e,ped}$ must be able to model its dependence on the effective mass A_{eff}.

Many studies using gyrokinetic codes have now demonstrated that electron-scale turbulence due to electron-temperature-gradient (ETG) driven modes and/or microtearing modes (MTMs) frequently dominates the heat transport across the H-mode pedestal (Told *et al*. 2008; Jenko *et al*. 2009; Hatch *et al*. 2015, 2016, 2017, 2019; Kotschenreuther *et al*. 2019; Hatch *et al*. 2021; Hassan *et al*. 2021), especially at high heating power and when the pedestal density gradient is steep.

Notably, Told *et al*. (2008) found, in their study on ASDEX-Upgrade, that, while MTMs were found to make the dominant contribution to the electron heat flux in the region just inside the pedestal top, small-scale ETG modes with maximum amplitudes near the 'x'-points were found to dominate in the steep-gradient region. They also pointed out, as was also in Jenko *et al*. (2009), that the measured values of the parameter $\eta_e \equiv L_{n_e}/L_{T_e} \sim 2$, where $L_{n_e} = n_e/(\mathrm{d}n_e/\mathrm{d}r)$ and $L_{T_e} = T_e/(\mathrm{d}T_e/\mathrm{d}r)$ are the electron temperature and density scale lengths, were a factor $\sim$1.6 above the linear threshold for ETG modes.

This observation of values of $\eta_e \sim 2$ across the pedestal was also reported in the earlier study by Neuhauser *et al*. (2002), on ASDEX Upgrade, in which it was suggested this might be related to the threshold behaviour of drift waves, and it was shown by Horton *et al*. (2005) that, by assuming a constant value of $\eta_e \sim 2$ across the pedestal, the measured T_e profile could be reconstructed from the n_e profile, leaving the electron temperature and density at the separatrix, $T_{e,sep}$ and $n_{e,sep}$, as the only other free parameters.

Several other studies have also revealed the importance of η_e in governing the electron heat flux q_e across the pedestal region (Guttenfelder *et al*. 2021; Chapman-Oplopoiou *et al*. 2022; Hatch *et al*. 2022) and have proposed several, rather similar scaling expressions for the gyro-Bohm normalised heat flux $q_e/q_{e,gB}$ with the parameters η_e and R/L_{T_e}. Here, the gyro-Bohm electron heat flux is defined as $q_{e,gB} = n_e \chi_{e,gB}\, T_e/R$, where the associated heat diffusivity $\chi_{e,gB} = v_{th,e}\rho_e^2/R$, $v_{th,e}$ is the electron thermal velocity and ρ_e is the electron Larmor radius.

A simplified heat flux scaling (or, alternatively, modified quasi-linear expressions for the ETG heat flux as proposed by Hatch *et al*. (2022)) can be used to form the basis of numerical models for the pedestal T_e profile. Such an approach is taken to construct the numerical model of pedestal structure developed by Guttenfelder *et al*. (2021), which is based on a combination of ETG heat transport governed by η_e and particle transport due to pressure-gradient-limited, kinetic-ballooning modes (KBMs) – consistent with the mechanisms for pedestal transport proposed by Hatch *et al*. (2016).

Such a simplified, semi-numerical model for the pedestal T_e profile, based on a scaling for the ETG-driven turbulent heat transport proposed in Chapman-Oplopoiou *et al*. (2022), appropriate for the steep-density gradient region of the H-mode pedestal, is presented in Field *et al*. (2023). Here, this model is used to predict the T_e profile across the pedestal of a set of 2 MA H-mode pulses, run in the JET tokamak with the beryllium wall and tungsten divertor (JET-Be/W) in which the effective isotope mass A_{eff} was varied from pure D to pure T, as well as pulses in D and T at higher and lower rates of gas fuelling (Frassinetti *et al*. 2023). Hence, the predictive capability of the model is tested both across the A_{eff} scan and at a different plasma current I_p and toroidal field B_t to that for which the scaling was determined, i.e. 2 MA/2.25 T rather than 1.4 MA/1.7 T, by comparing the predicted values of T_e with those measured at two locations at the top of the T_e and n_e pedestals.

The resulting agreement between the predicted and measured values of T_e at the top of the density pedestal provides strong evidence that the electron heat transport across the steep-density gradient region of the pedestal conforms to the assumed scaling for $q_e/q_{e,gB}$ with η_e, which is independent of the ion mass and hence of A_{eff}. Furthermore, the applicability of this model also highlights the importance of the pedestal boundary conditions at the separatrix, i.e. $n_{e,sep}$ and $T_{e,sep}$ in governing the pedestal temperature $T_{e,ped}$, which is a consequence of the assumed electron heat flux dependence on η_e.

By combining the ETG critical-heat-flux model of Field *et al*. (2023) with the EPED model of Snyder *et al*. (2009) for prediction of the total pressure at the pedestal top p_{ped}, we demonstrate in § 6 that it is also possible to predict the pedestal ion temperature $T_{i,ped}$, although this also requires knowledge of $n_{e,ped}$. Furthermore, by combining these two models with the density-pedestal (DP) prediction model of Saarelma *et al*. (2023) for $n_{e,ped}$, it is possible to obtain a full prediction of the pedestal n_e, T_e and T_i profiles, only requiring the boundary conditions at the separatrix ($n_{e,sep}$ and $T_{e,sep}$) and the heat flux (P_{sep}/S, where P_{sep} is the loss power across the separatrix and S is the area of the LCFS) across the pedestal as the main experimental inputs.

The remainder of this paper is structured as follows: the ETG model for the pedestal T_e profile is outlined in § 2, then the experimental § 3 describes the pedestal data set used for this comparison in § 3.1, followed by an explanation of how the data are prepared for input to the model in § 3.2. The resulting comparisons of the predicted and measured T_e profiles are then presented in § 4, followed by a discussion

of these comparisons in terms of current understanding of the underlying physics of turbulent electron heat transport across the pedestal in § 5. Results from attempts to combine the ETG model for the pedestal T_e profile with the EPED model of Snyder *et al*. (2009) for the pedestal height and width are presented in § 6. The overall conclusions of the study are then summarised in § 7.

2. The ETG heat transport model for pedestal T_e profile

The model of Field *et al*. (2023) is based on a scaling for the gyro-Bohm normalised turbulent electron heat flux $Q_e^\star \equiv q_e/q_{e,MgB}$ with the parameter $\eta_e = L_{n_e}/L_{T_e}$. Here, the modified gyro-Bohm normalisation $q_{e,MgB} = q_{e,gB}(R/L_{T_e})^2$ is defined in terms of the local L_{T_e} at the simulated flux surface within the pedestal region, rather than the usual definition in terms of a macroscopic length scale such as the major radius of the plasma R.

The $Q_e^\star(\eta_e)$ scaling was determined as a fit to saturated, turbulent electron heat-flux q_e data from a set of local, nonlinear, electromagnetic, electron-scale simulations, which were performed by Chapman-Oplopoiou *et al*. (2022) using the gyrokinetic (GK) code GENE (Jenko 2000; Goerler *et al*. 2011). The simulations were run at a flux surface in the steep-density gradient region of the pedestal, half way between the density pedestal top (defined here in terms of the normalised poloidal flux as $\psi_N^{n_{e,top}}$) and the separatrix (at $\psi_N = 1$).[1]

Two sets of pedestal profiles were considered from 1.4 MA JET-Be/W deuterium pulses at high and low rates of gas fuelling ($\Gamma_{D2} \sim 0.3$ and $1.8 \times 10^{22}\,\mathrm{es}^{-1}$) with 16 MW of heating power, which were run during experiments performed by Maggi *et al*. (2015, 2017). For each set of pedestal profiles, simulations were run with the normalised density and temperature gradients R/L_{n_e} and R/L_{T_e} scanned around their nominal experimental values (Chapman-Oplopoiou *et al*. 2022).

It was found that by defining $Q_e^\star \equiv q_e/q_{e,MgB}$ in terms of the local L_{T_e} rather than the major radius R, the q_e data from all four gradient scans could be fitted approximately by the same $Q_e^\star(\eta_e)$ scaling

$$Q_e^\star = \alpha(\eta_e - \eta_{e,cr})^\beta, \tag{2.1}$$

where $\alpha = 0.85$, $\eta_{e,cr} = 1.28$ and $\beta = 1.43$. Here, the threshold $\eta_{e,cr}$ is somewhat higher than the linear threshold of 0.8 found, e.g. in Jenko, Dorland & Hammett (2001) for ETG turbulence.

The heat-flux scaling of (2.1) is used as the basis for the numerical model described in Field *et al*. (2023). Note that it is similar to the electron heat-flux scaling found by Guttenfelder *et al*. (2021) from a set of nonlinear GK simulations using the CGYRO code (Candy, Belli & Bravenec 2016) for the steep-density gradient region of a set of DIII-D pedestals, which is also used for numerical calculation of the pedestal T_e profile, as described in Guttenfelder *et al*. (2021).

Numerical calculation of the pedestal T_e profile is performed as follows: first, by assuming a linear form of (2.1), i.e. with $\beta = 1$, it can be expressed in the form of the cubic polynomial in R/L_{T_e}

$$(R/L_{n_e})^{-1}(R/L_{T_e})^3 - \eta_{e,cr}\,(R/L_{T_e})^2 - q_e/(\alpha q_{e,gB}) = 0, \tag{2.2}$$

which can be solved for R/L_{T_e} at any flux surface given values of q_e, T_e, the magnetic field B and n_e and R/L_{n_e}. This solution then provides an initial estimate of R/L_{T_e},

[1] The normalised poloidal flux is defined as $\psi_N = (\psi - \psi_0)/(\psi_a - \psi_0)$, where ψ, ψ_0 and ψ_a are the values of poloidal flux at an arbitrary flux surface, the magnetic axis and the separatrix, respectively.

which is subsequently used to perform a more accurate, numerical solution of the nonlinear form of the heat-flux scaling described by (2.1) with $\beta = 1.43$. The electron heat flux q_e is determined from $q_e = P_{e,sep}/S$, where $P_{e,sep}$ is the loss power conducted across the pedestal by the electrons and S is the area of the LCFS. The T_e profile across the pedestal is calculated by applying the above method to solve for R/L_{T_e} iteratively, starting at the separatrix, where $T_e = T_{e,sep}$, using the prescribed, fitted experimental density profile to provide n_e and R/L_{n_e} and taking T_e from the previous iteration step. A more detailed explanation of the numerical algorithm can be found in Field *et al*. (2023).

3. Experimental data set and data preparation

3.1. *Isotope mix and gas fuelling rate scans at constant β_N*

The experimental data set used for this comparison is from a series of type-I ELMy H-mode plasmas, i.e. plasmas with type-I Edge-Localised Modes, with plasma current $I_p = 2$ MA at a toroidal field $B_t = 2.25$ T in JET-Be/W, over which the effective mass A_{eff} was scanned from pure deuterium (D) to pure tritium (T) (Frassinetti *et al*. 2023). The equilibrium configuration positioned the inner strike point on the vertical target and outer strike point on the horizontal target with a plasma cross-section of low average triangularity ($\delta \sim 0.24$).

Over the scan, the key parameters that affect the pedestal behaviour (normalised pressure $\beta_N \sim 1.5$, ratio of the separatrix density to the pedestal density $n_{e,sep}/n_{e,ped}$, pedestal ion Larmor radius $\rho_i \sim 2.1{-}2.3 \times 10^{-3}$, pedestal electron collisionality $\nu_e^\star \propto n_e/T_e^2$ and toroidal rotation rate Ω_ϕ^{ped}) were kept as constant as possible. Feedback control of the neutral beam injection (NBI) heating power was used to maintain $\beta_N \sim 1.44 - 1.58$, while the ion-cyclotron-resonance (ICRH) heating was maintained at 2 MW. It was not possible to maintain a constant value of pedestal collisionality $\nu_e^\star$, which varied from ∼0.8 in D to ∼1.8 in T (Frassinetti *et al*. 2023).

The A_{eff} scan, comprising six pulses (two in pure D, three in mixed D and T and one in pure T), was performed at a gas fuelling rate $\Gamma_{gas} \sim 1.7 \times 10^{22}$ es^{-1}, injected from divertor. In all pulses, a small H concentration ($c_H \sim 1$ %) was used for the minority ICRH heating. At this fuelling rate, the ratio of density at the separatrix to that at the pedestal top was maintained at $n_{e,sep}/n_{e,ped} \sim 0.5$.

In order to investigate the role of the ELM frequency f_{ELM} on the pedestal structure, in particular the density ratio $n_{e,sep}/n_{e,ped}$, further pulses (referred to as the 'extended data set' in Frassinetti *et al*. (2023)) were run at higher and lower gas fuelling rates (two in D and two in T), the higher gas rate promoting more frequent ELMs. The importance of $n_{e,sep}/n_{e,ped}$ in determining the cross-pedestal transport is discussed in detail in Frassinetti *et al*. (2021). The parameters of the full set of pulses used for this study are summarised in table 1 of Appendix A.

3.2. *Input data and data preparation*

Required inputs for calculation of the pedestal T_e profile using the model described in § 2 are: the nominal toroidal magnetic field B_t, the separatrix loss power during the inter-ELM periods P_{sep}^{iELM} and the fraction of this power carried by the electrons $f_{cnd,e}$ and the measured n_e profile across the pedestal, together with the corresponding T_e profile for comparison with the predicted profile.

The pre-ELM, pedestal kinetic profiles used for these comparisons are fits of mtanh() functions (Groebner *et al*. 2001) to an ensemble of n_e and T_e profile data measured by the JET-Be/W high-resolution Thomson scattering (HRTS) system

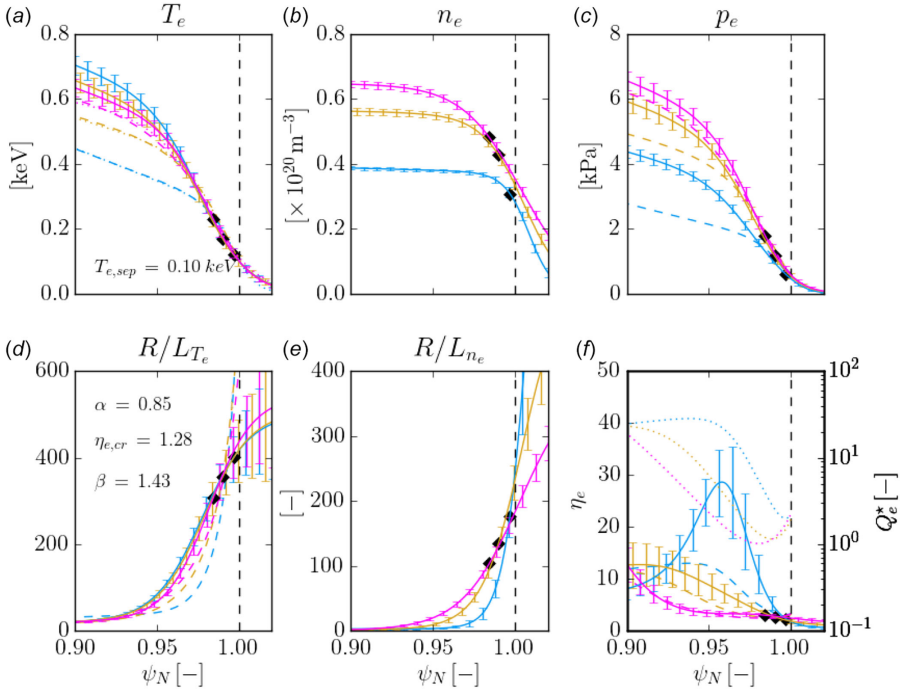

FIGURE 1. *Pre-ELM averaged* (∼80 % to 100 % *of the inter-ELM period*) *pedestal profiles for three* 2 MA *JET-Be/W H-mode pulses in pure D* (*no. 99208*, *blue*), *pure T* (*no. 100247*, *gold*) *and a D:T isotope mixture with an effective mass* $A_{eff} \sim 2.4$ (no. *99491*(*a*), *magenta*) *at a nominal hydrogenic gas fuelling rate of* $\Gamma_{gas} \sim 1.6 \times 10^{22}\ \mathrm{es}^{-1}$, *with other pulse parameters given in table 1*, *showing:* (*a*) *electron temperature* T_e, (*b*) *density* n_e, (*c*) *pressure* p_e, *their normalised gradients* (*d*) R/L_{T_e}, (*e*) R/L_{n_e} *and* (*f*) *the parameter* η_e (*solid/dashed*) *and the locally gyro-Bohm normalised electron heat flux* $Q_e^\star$ (*dotted*) *vs normalised poloidal flux* ψ_N. *In* (*a–c*), *input profiles from the EUROfusion pedestal database are shown by the solid lines with error bars; in* (*a*) *the* T_e *profile calculated using the ETG model is shown by the dashed lines, while* mtanh() *fits to these profiles are shown by dotted lines* (*note that the fits overlay the calculated* T_e *profiles, resulting in the dot-dashed lines*); *in* (*c, d & f*) *profiles of derived quantities* (p_e, R/L_{T_e} and η_e), *calculated using the* T_e *profile from the ETG model are shown by the dashed lines. The* ♦ *symbols indicate the 'mid-pedestal' positions.*

(Pasqualotto *et al*. 2004). The finite spatial resolution of the HRTS measurements is taken into account in the fitting procedure as described in Frassinetti *et al*. (2012). The ensemble of measurements are for HRTS laser pulses (with 50 ms) repetition rate) that fall within the last 20 % of the ELM cycle, i.e. the fraction 0.8–1.0 of the relative inter-ELM period τ_{ELM}, which occurs during the averaging time windows $t_0 - t_1$ specified in table 1.

The resulting fitted profiles and the measured profile data are stored, together with the parameters of the mtanh() fits and their uncertainties, in the JET processed-pulse files (PPFs), also specified in table 1. These files form a subset of the JET-processed, EUROfusion Pedestal Database (Frassinetti *et al*. 2021). The fitted profiles, e.g. as shown in figure 1(*a–c*) are reconstructed from the parameters of the mtanh() function using a Monte Carlo method to calculate uncertainties on the profiles and also on the derived gradient parameters R/L_{T_e}, R/L_{n_e} and η_e. In order to set the

temperature at the separatrix $T_{e,sep}$ at a prescribed value, the T_e profiles are shifted radially in ψ_N, with the same shift applied to the n_e and p_e profiles.

The separatrix temperature is a rather 'stiff' parameter, scaling approximately as $T_{e,sep} \propto P_{e,sep}^{2/7}$ (Stangeby 2000) and is found, e.g. from calculations using a Scrape-off-Layer (SOL) model to vary only within a rather limited range of $80-110$ eV on JET-Be/W for a wide range of $P_{e,sep}$ (Simpson *et al*. 2019). Hence, the fixed value of $T_{e,sep} = 100$ eV is assumed for all of the cases considered here.

Calculation of the time-averaged, conducted loss power across the pedestal during the inter-ELM periods P_{sep}^{iELM} requires subtracting the radiated power from the confined plasma P_{Rad}^{iELM} and the time-averaged ELM loss power $\langle P_{ELM} \rangle$ from the absorbed heating power P_{abs} i.e. $P_{sep}^{iELM} = P_{abs} - P_{Rad}^{iELM} - \langle P_{ELM} \rangle$. Here, the absorbed heating power P_{abs} is the sum of the injected NBI power, the ICRH heating power and the ohmic power minus the shine-through power $P_{abs} = P_{NB} + P_{RF} + P_{OH} - P_{sh}$; the radiated power P_{Rad}^{iELM} is determined from tomographic reconstructions of multi-channel bolometric measurements of the total radiation and the ELM loss power from the rate of change of the total stored energy of the plasma $\mathrm{d}W_{pl}/\mathrm{d}t$ between the ELMs determined from magnetic equilibrium reconstructions. The methodology of this analysis of the loss power is exactly the same as used in Field *et al*. (2020), to which the reader is referred for further details.

The results presented here have been calculated assuming that the total heat flux conducted across the pedestal during the inter-ELM periods $q_{cond} = P_{sep}^{iELM}/S$, where S is the area of the LCFS, is carried by the electrons, i.e. $f_{cnd,e} = 1$. For the JET-Be/W equilibria used here, the area of the LCFS formed by the separatrix $S \sim 140\,\mathrm{m}^2$. Calculated values of P_{abs}, P_{Rad}^{iELM}, $\langle P_{ELM} \rangle$ and the resulting P_{sep}^{iELM} are given for each of the cases in table 1. It is interesting to note that, while the variation of heating power P_{abs} required to maintain constant β_N is quite small, i.e. $\sim$12$-$18 MW ($\pm$20 %), the ranges of $P_{Rad}^{iELM} \sim 3-7$ MW ($\pm$40 %)) and $\langle P_{ELM} \rangle \sim 0.5-9$ MW ($\sim \pm 50$ %)) are much larger and roughly compensate one another, resulting in a smaller variation of $P_{sep}^{iELM} \sim 5-8$ MW ($\sim \pm 33$ %).

Note that the predicted pedestal temperature from the model scales approximately as $(T_{e,ped}^{ETG} \propto (P_{sep}^{iELM} B_t^2)^{1/3}$, so is rather insensitive to the loss power, i.e. $\delta T_{e,sep}/T_{e,sep} \sim (\delta P/P)/3$. It has been found that $T_{e,ped}$ is much more sensitive to other input parameters, in particular the assumed temperature at the separatrix $T_{e,sep}$ and the nonlinear threshold $\eta_{e,cr}$ of the assumed ETG heat-flux scaling. Hence, uncertainties in P_{sep}^{iELM} are not quoted in table 1 or propagated to give uncertainties on the predicted $T_{e,ped}^{ETG}$.

4. Comparisons of predicted and measured T_e profiles

A comparison of the measured pedestal profiles for cases in pure D and T and an mixed D:T case with $A_{eff} \sim 2.4$ at the same gas fuelling rate of $\Gamma_{gas} \sim 1.6 \times 10^{22}\,\mathrm{es}^{-1}$ is shown in figure 1(*a–c*) (solid), from which it can be seen that the pedestal density $n_{e,ped}$ increases with A_{eff}, while the temperature $T_{e,ped}$ only slightly decreases with A_{eff}, resulting in an overall increase in $p_{e,ped}$, as is discussed in Frassinetti *et al*. (2023). This result is also consistent with other isotope mass scans in JET-Be/W, e.g. as reported in Schneider *et al*. (2023).

Both the normalised temperature and density gradients increase strongly with radius to values $\mathcal{O}(100)$ at the separatrix from much lower values $R/L_{T_e} \sim \mathcal{O}(10)$ and $R/L_{n_e} \sim \mathcal{O}(1)$ inside the pedestal top. In the steep-density gradient region close

to the separatrix, the parameter η_e has a value $\sim$2, increasing strongly at and inside the density pedestal top, where the n_e gradient is weak.

For this data set, which is based on performing mtanh() fits to the HRTS data only, as well as $n_{e,ped}$ increasing, the width of the density pedestal also increases and shifts inwards with increasing effective mass A_{eff}. However, it should be noted that the pedestal profile data presented in Frassinetti *et al*. (2023) were obtained by fitting a revised form of the mtanh() function (Frassinetti *et al*. 2016) also incorporating a finite slope in the outer, low-field-side SOL region as well in as the core, high-field-side region of the pedestal to n_e profile data obtained by combining that from both the HRTS and the Li-beam diagnostic (Réfy *et al*. 2018), as described in Frassinetti *et al*. (2016).

The Li-beam provides more detailed, reliable n_e measurements than available from the HRTS system over the SOL region, where the scattered signal is weak. This change primarily affects the fits in the SOL region, in particular for the cases at high gas fuelling rates, for which the outward relative shift of the n_e profile is largest, decreasing the fitted pedestal width Δ_{n_e} and slightly increasing the n_e gradient inside the separatrix in comparison with the values obtained with the standard mtanh() fit. For this reason, the reader is referred to Frassinetti *et al*. (2023) for definitive statements regarding the dependence of the pedestal structure on A_{eff}.

The density at the separatrix $n_{e,sep}$ varies similarly to $n_{e,ped}$ with A_{eff}, so the density ratio $n_{e,sep}/n_{e,ped}$ remains approximately constant. These trends are also plotted explicitly for the full data set in figure 2, in which the colour scale represents the gas fuelling rate Γ_{gas}.

The predicted T_e and p_e profiles, calculated using the ETG model described in § 2 are shown in figures 1(*a*) and 1(*c*) (dashed). Comparing the measured and predicted profiles, it can be seen that these match well in the steep-density gradient region between the separatrix and the density pedestal top, while further inwards, where the density gradient is weak and η_e is large, the predicted T_e under-predicts the actual value.

At the mid-pedestal location, half-way between the density pedestal top and the separatrix (indicated in the figure by the ♦), for which the heat-flux scaling of (2.1) was determined from the nonlinear GENE simulation results, the predicted value of R/L_{T_e} closely matches the actual value, while further outwards R/L_{T_e} is over-predicted and under-predicted further inwards. In other words, the electron heat flux q_e determined from the $Q_e^\star$ scaling is too high inside the mid-pedestal location and too low further outwards, requiring too low and too high a temperature gradient T_e' to match the prescribed q_e.

In figure 2(*a*), the predicted pedestal temperature $T_{e,ped}^{ETG}$ (indicated by the •) is plotted as a function of the measured $T_{e,ped}$ for the full data set from both the effective mass and gas rate scans. From this, it is evident that, for most but not all cases, the model under-predicts $T_{e,ped}$ compared with the measured values, in some cases by over a factor $\sim$2. The degree of agreement appears to be independent of the particular gas fuelling rate Γ_{gas} used.

The position of the T_e pedestal top $\psi_N^{T_{e,top}}$ is generally located further inwards to that of the density pedestal top $\psi_N^{n_{e,top}}$, i.e. there is a relative inward shift of the T_e profile, $\delta_{n-T} = \psi_N^{n_{e,top}} - \psi_N^{T_{e,top}}$, which has been well documented in previous studies (Frassinetti *et al*. 2021) and found to be well correlated with the increasing density ratio $n_{e,sep}/n_{e,ped}$ resulting from higher rates of gas fuelling. A consequence of this inward shift of the T_e pedestal top relative to that of the density is that an increasing

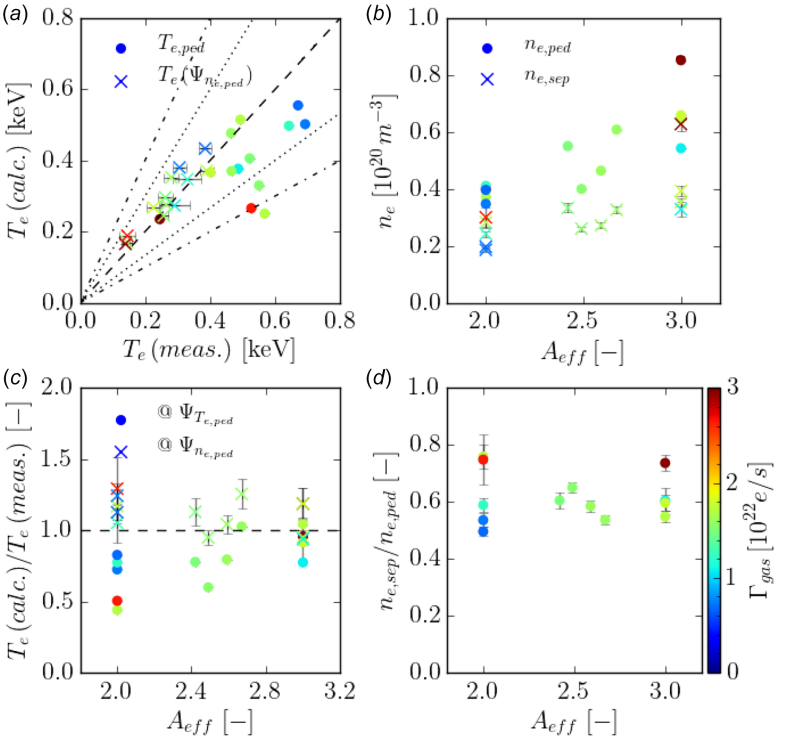

FIGURE 2. *Calculated and measured pedestal parameters corresponding to the cases for the isotope mix and fuelling rate scans for the* 2 MA *H-mode pulses listed in table 1, showing:* (*a*) $T_{e,ped}$ *from the* mtanh() *fit* (•) *and* T_e *at the location of the density pedestal top* $T_e(\psi_N^{n_{e,top}})$ (×), *both calculated using the ETG model, vs the equivalent experimental values* (*calculated values of* T_e *at factors of 1.5 and 2 higher/lower than the measured values are represented by the dotted and dot-dashed lines respectively*); (*b*) $n_{e,ped}$ (•) *and* $n_{e,sep}$ (×) *vs the effective isotope mass ratio* A_{eff}; (*c*) *the ratios of* T_e *calculated using the ETG model to the measured values at* $\psi_N^{T_{e,top}}$ (•) *and at* $\psi_N^{n_{e,top}}$ (×); *and* (*d*) *the separatrix to pedestal density ratio* $n_{e,sep}/n_{e,ped}$ *vs* A_{eff}, *where the colour represents the gas fuelling rate* Γ_{gas} es^{-1}.

portion of the T_e pedestal is coincident with the region of weak-density gradient inside the density pedestal top, i.e. in this inner region of the pedestal R/L_{T_e} well exceeds R/L_{n_e} and η_e is consequently large.

It is sometimes stated as an explanation of the lower $T_{e,ped}$ resulting from the relatively high gas fuelling rates for sustained, high-power operation on JET-Be/W (Giroud *et al*. 2013), that the resulting higher values of η_e across the region of weak-density gradient at the pedestal top drives more turbulent heat transport and hence cools the pedestal (Frassinetti *et al*. 2019). However, the loss power conducted across the pedestal $P_{e,sep}$ is prescribed, the T_e gradient at a particular location adjusting to drive the corresponding turbulent electron heat flux q_e. Furthermore, we learn from the above discussion that our $Q_e^\star$ scaling for the electron heat flux determined for the steep-density gradient region actually over-predicts q_e in this region of weak-density gradient, so whatever branch of turbulence is prevalent there requires a higher rather than lower driving T_e gradient to match the prescribed heat flux. This point is discussed further in § 5 below.

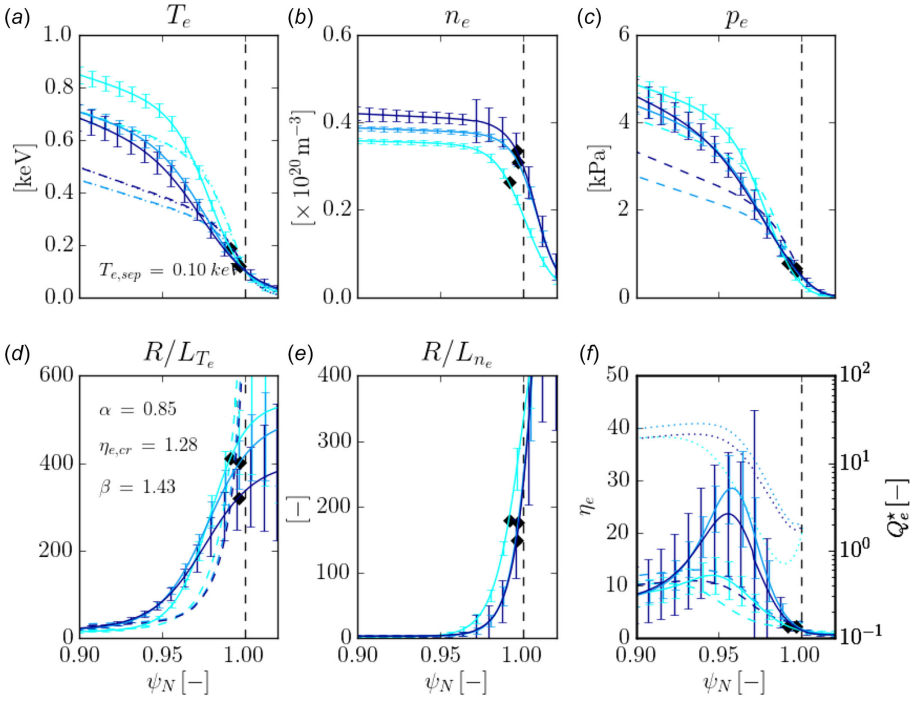

FIGURE 3. *Pedestal profiles for the three* 2 MA *JET-Be/W H-mode deuterium pulses* ($A_{eff} = 2$) *from table 1* no. *96202* (*cyan*), *no. 96208* (*mid-blue*) *and no. 96201* (*dark-blue*) *with gas fuelling rates of* $\Gamma_{gas} \sim 0.74$, 1.7 and 2.7×10^{22} es^{-1}, *respectively, with the plotted quantities as defined in figure 1*.

Values of the predicted T_e at the location of the density pedestal top $T_e(\psi_N^{n_{e,top}})$ are also plotted (as the $\times$'s) in figure 2(*a*) as a function of the corresponding measured values at the same location. It is evident that there is a much better agreement between the model prediction and the measured values at this location than at the T_e pedestal top, with only a slight over-prediction of $T_e(\psi_N^{n_{e,top}})$ by factor $\lesssim 1.2$. This is to be expected because the $Q_e^\star$ scaling on which the model is based was determined from the nonlinear GENE simulations for the steep-density gradient and prediction of $T_e(\psi_N^{n_{e,top}})$ requires calculation of T_e over this region but not further inwards of the density pedestal top where the density gradient is weak.

The effect of increasing the gas fuelling rate Γ_{gas} in both the pure D and pure T pulses is shown in figures 3 and 4, respectively. For the D pulses, increasing Γ_{gas} by a factor of $\sim$3.5 results in only a small increase in $n_{e,ped}$, i.e. the gas fuelling is rather inefficient at fuelling the confined plasma. In fact, the increased fuelling results in a higher ELM frequency and these then expel the additional particles deposited inside the separatrix at an increased rate, almost balancing the additional influx.

The main effect of the increased gas rate is to increase the density at the separatrix and hence the density ratio $n_{e,sep}/n_{e,ped}$, as is also shown in figure 2(*c*). This has the effect of shifting the n_e profile outwards with respect to the T_e profile, thereby narrowing the steep-density gradient region just inside the separatrix and increasing η_e at the pedestal top, as is also discussed in Frassinetti *et al*. (2019).

In the case of the two D pulses no. 96208 and no. 96201 shown in figure 3 at the two higher fuelling rates of 1.7 and 2.7×10^{22} es^{-1} for which f_{ELM} is particularly

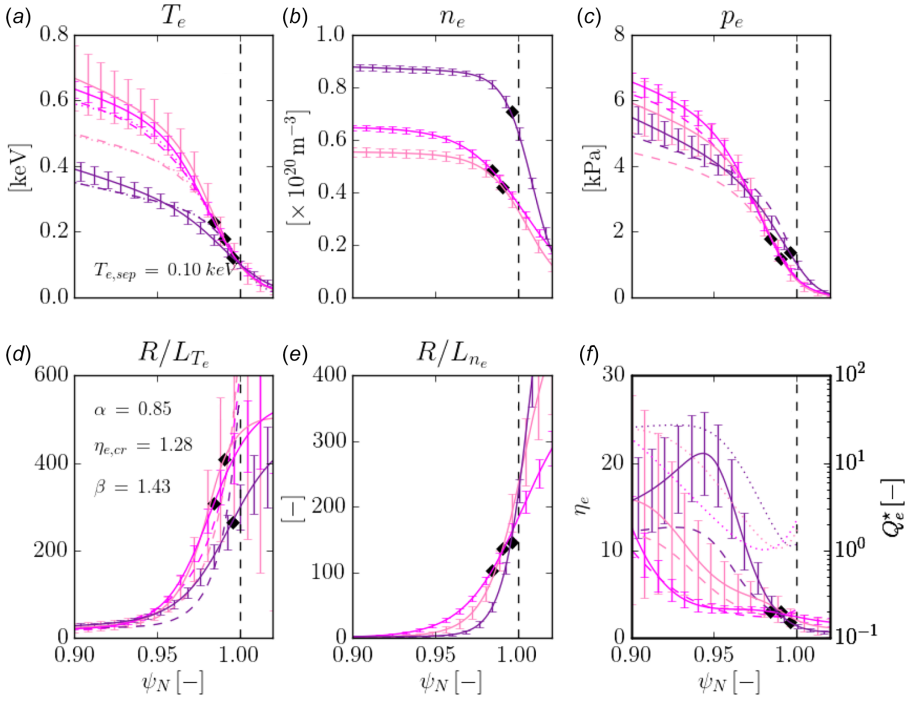

FIGURE 4. *Pedestal profiles for the three* 2 MA *JET-Be/W H-mode tritium pulses* ($A_{eff} = 3$) *from table 1* no. *100185* (*pink*), *no. 100247* (*magenta*) *and no. 100183* (*purple*) *with gas fuelling rates of* $\Gamma_{gas} \sim 1.1$, 1.7 and 3.0×10^{22} es^{-1}, *respectively, with the plotted quantities as defined in figure 1*.

high ($\gtrsim 70$ Hz), the degree of agreement between the predicted value of $T_{e,ped}$ and the measured value is particularly poor.

Similar trends are observed for the T as for the D pulses, except that the pulse no. 100183 at the highest fuelling rate of 3.0×10^{22} es^{-1} has an anomalously high pedestal density, increasing more strongly for a similar increase in Γ_{gas} than in the case of the D pulse no. 96201 shown in figure 3. This increase can be attributed to the low ELM frequency in pulse no. 100183 of $f_{ELM} \sim 7.5$ Hz, which is much lower than in the other pulses in the data set.

Hence, in the T pulses, the effect of increasing the gas fuelling is not to increase but to decrease f_{ELM}. In the case of the T pulses, increasing Γ_{gas} increases the radiated power P_{Rad}^{iELM} and hence the rate at which the pedestal energy $W_{e,ped}$ can increase between the ELMs, thereby decreasing f_{ELM} and the ELM power loss $\langle P_{ELM} \rangle$. However, for the D pulses, increasing Γ_{gas} has the opposite effect of reducing P_{Rad}^{iELM}, which increases rather than decreases f_{ELM}.

These observations support the notion that the narrower the steep-density gradient region, the worse the predictive capability of the model, which is not applicable to the weak-density gradient region inside the density pedestal top. The particularly poor agreement for the T pulse no. 100183 at the highest fuelling rate also follows this trend. Note that the dependencies of the loss power components due to radiation, ELMs and inter-ELM heat transport across this data set are discussed in more detail in Frassinetti *et al*. (2023).

Generally, as is evident from figure 2(*a*), the higher gas fuelling rates, with the correspondingly higher density ratios $n_{e,sep}/n_{e,ped}$ exhibit the lowest values of $T_{e,ped}$ and $T_e(\psi_N^{n_{e,top}})$, in agreement with several previous studies on JET-Be/W, e.g. as in Frassinetti *et al*. (2019, 2021). An alternative interpretation of this observation to that proposed in Frassinetti *et al*. (2019), i.e. increased turbulent transport due to higher resulting values of η_e across the pedestal, is discussed in § 5.

5. Discussion

In the following sections, several aspects of the pedestal heat transport are discussed: in § 5.1, the important role of the separatrix boundary conditions in determining the pedestal structure; in § 5.2, the expected dependencies of the pedestal T_e profile on the toroidal field B_t and the effective isotopic mass A_{eff}, which is indirect through it's dependence on the n_e profile; and in § 5.3, the expected threshold for the ETG turbulence on pedestal gradients in terms of R/L_{T_e} and R/L_{n_e} or η_e. There follows in § 5.4, a brief review of GK studies of the structure of the pedestal turbulence, which highlights the dominant contribution of 'slab'-like, electron-temperature-gradient-driven (S-ETG) turbulence to the heat flux across the steep gradient region of the pedestal.

5.1. *On the role of the separatrix boundary conditions*

An extreme simplification of the model for the pedestal T_e profile presented in § 2 gives insight into the important role that the density ratio $n_{e,sep}/n_{e,ped}$ plays in governing the resulting pedestal temperature, in particular its value at the density pedestal top $T_e(\psi_N^{n_{e,top}})$. As reported in Field *et al*. (2020), values of the parameter η_e averaged over the steep-density gradient region of the pedestal is often observed to saturate at a value $\langle\eta_e\rangle_{ped} \sim 2$ in JET-Be/W plasmas. This observation is also supported by results presented in Frassinetti *et al*. (2023).

It is also discussed in Guttenfelder *et al*. (2021), that values of $\langle\eta_e\rangle_{ped}$ in the range 1–2 have been reported on several other devices and it is explicitly mentioned in Jenko *et al*. (2009) that values of $\eta_e \sim 2$ measured across the steep-density gradient region in ASDEX Upgrade pedestals lie at $\sim$1.6$\times$ the linear threshold and that this observation might be attributable to the 'stiffness' of turbulent ETG-driven heat transport. Similar observations from ASDEX Upgrade were also reported earlier in Neuhauser *et al*. (2002) and in Horton *et al*. (2005) it was shown that the pedestal T_e profile could be reconstructed from the n_e profile by assuming a constant $\eta_e \sim 2$, in accordance with the following discussion.

In Field *et al*. (2020), the consequences of assuming that infinitely 'stiff' electron heat transport clamps η_e to a constant, critical value $\bar{\eta}_e$ across the pedestal are discussed. Under this assumption, the definition of $\eta_e \equiv L_{n_e}/L_{T_e}$ represents a first-order differential equation $T_e'/T_e = \bar{\eta}_e(n_e'/n_e)$, where the prime $' = d/dr$. On integration inwards from the separatrix, this yields the following simple relation for T_e at the top of the density pedestal:

$$T_e(\psi_N^{n_{e,top}}) = T_{e,sep}\left(\frac{n_{e,ped}}{n_{e,sep}}\right)^{\bar{\eta}_e}. \tag{5.1}$$

This highlights the importance of the boundary conditions at the separatrix for the case of stiff heat transport, i.e. that $T_{e,ped}$ is then proportional to $T_{e,sep}$ and increases strongly with the density ratio $n_{e,ped}/n_{e,sep}$, conversely decreasing with the inverse ratio $n_{e,sep}/n_{e,ped}$. This can be understood from the n_e in the denominator on the right-hand side of the initial differential equation, which results in a larger value of

T_e' for given values of R/L_{n_e} and T_e at the separatrix, this increase then propagating inwards as the temperature profile is integrated.

Hence, taken together, the observation that across the steep-density gradient region of the pedestal $\langle \eta_e \rangle_{ped} \sim 2$ and the simplifying assumption of infinitely stiff electron heat transport, offers an explanation of the decreasing dependence of $T_{e,ped}$ on the density ratio $n_{e,sep}/n_{e,ped}$. Furthermore, in the density pedestal prediction model of Saarelma *et al*. (2023), which is discussed further in § 6.1 below, the pedestal density is also strongly dependent on the separatrix density.

5.2. *Influence of the effective isotope mass A_{eff} and B-field*

The heat-flux scaling of (2.1) on which the model described in § 2 is based is only dependent on the electron mass m_e appearing in the gyro-Bohm normalisation $q_{e,gB} \propto \rho_e^2 \propto m_e$, so is independent of the isotopic mass A_{eff} of the plasma ions. However, the predicted pedestal T_e profile does depend on the density profile, which does vary with A_{eff}, as is described in detail in Frassinetti *et al*. (2023). Across the data set used here and in Frassinetti *et al*. (2023), $n_{e,ped}$ increases by ∼50 % when changing isotope from pure D to T, i.e. with A_{eff} increasing from 2 to 3, while $T_{e,ped}$ decreases by ∼25 %. As shown in figures 2(*b*) and 2(*c*), $n_{e,sep}$ increases with A_{eff}, although less than $n_{e,ped}$, resulting in an almost constant density ratio $n_{e,sep}/n_{e,ped}$.

The effect of these changes to the density profile is that the model predictions for $T_{e,ped}$ broadly reproduces the observed trends. As described above, the effect of increasing the assumed $n_{e,sep}$ is to decrease the initial T_e gradient at the separatrix, so results in lower predicted T_e across the whole pedestal. At each flux surface, the predicted R/L_{T_e} adjusts to give the appropriate η_e required to match the prescribed electron heat flux q_e, accounting for the predicted, local value of the gyro-Bohm normalisation $q_{e,MgB}$.

As can be seen from figure 2(*a*), the predicted T_e at the density pedestal top $T_{e,ped}^{ETG}(\psi_N^{n_{e,top}})$ typically agrees quite well with the measured values. The ratios of the calculated to measured values shown in figure 2(*c*) show that the predicted values overestimate the measured values by up to a factor ∼1.2. This indicates that, at least across the steep-density gradient region of the pedestal, the electron heat transport is probably independent of A_{eff}.

As is also evident from figure 2(*c*), the agreement between the predicted and measured values of $T_{e,ped}$ improves with increasing A_{eff}, i.e. is better for the T pulses with lower $T_{e,ped}$ than for the D pulses. This indicates that the underlying scaling for the electron heat transport across the weak-density gradient region must depend to some extent on A_{eff}.

This trend is consistent with the electron heat flux across the weak-density gradient region having a significant component due to ion-scale turbulence, which does exhibit a dependence on isotope mass. For example, the ion gyro-Bohm normalisation $q_{i,gB}$ scales with A_{eff}. So, should the heat transport require a relatively constant normalised heat flux $q_e/q_{i,gB}$, this alone would result in the predicted $T_{e,ped}$ decreasing with A_{eff}. Furthermore, the ion mass can affect the growth rates of trapped-electron-driven-mode (TEM) turbulence by changing the electron–ion collision frequency, which increases with $A_{eff}^{1/2}$. This would reduce the trapped-electron fraction for otherwise similar parameters and hence decrease the linear growth rates of TEM modes.

Global linear GK simulations using GENE, discussed in Frassinetti *et al*. (2023) performed without flow shear, yielded lower growth rates for ion-scale turbulence

with $k_y \rho_i \lesssim 0.4$ and a significant TEM component for the T pulse no. 100247 compared with the D pulse no. 96208, while in simulations with flow shear, the ion-scale turbulence is completely suppressed in the T pulse but not in the D pulse. As TEM turbulence is thought responsible for electron particle transport (Kotschenreuther *et al*. 2019), this change is consistent with the higher $n_{e,ped}$ of the T pulse. In this case there would be an indirect effect of increasing A_{eff} on $T_{e,ped}$. Should the pedestal heat transport be dominated by ETG turbulence, as it is across the steep-density gradient region, the increased pedestal density would then result in a reduction of T_e across the pedestal.

In a recent detailed GK study of Predebon *et al*. (2023) of the isotope mass dependence of pedestal transport in three 1.4 MA, low-triangularity ($\delta \sim 0.2$) JET-Be/W pulses, two in D and one in H at similar fuelling rates, local ρ_e-scale GK simulations using GENE revealed that heat transport due to ETG turbulence dominates near the pedestal top, decreasing in significance outwards towards the separatrix. Swapping the isotope mass in the simulations, resulted in a negligible change in the predicted heat fluxes, showing that ρ_e-scale ETG turbulence is unable to explain the isotope effect on the heat transport. Also, as expected for ETG turbulence, the predicted particle and ion heat fluxes were negligibly small.

In the global ρ_i-scale GK simulations of Predebon *et al*. (2023), the turbulent ion heat transport was found to be mostly due to ion-temperature-gradient (ITG) driven modes and to be characterised by an anti-gyro-Bohm heat-flux scaling due to different normalised $E \times B$ shearing rates in species units $\tilde{\omega}_{E\times B}(H) = A_D^{-1/2} \tilde{\omega}_{E\times B}(D)$, relevant for flow–shear stabilisation of the ion-scale turbulence. Here, the normalised $E \times B$ shearing rate is defined as $\tilde{\omega}_{E\times B} = \omega_{E\times B}/(c_i/a)$, where c_i is the ion sound speed and a is the minor radius. As the neo-classical (NC) transport component of the ion heat flux is instead characterised by a gyro-Bohm scaling, overall this resulted in no net isotope dependence of the ion heat transport.

Turning to particle transport, whereas the NC component is not expected to be affected by the isotope mass, the global ρ_i-scale GK simulations of Predebon *et al*. (2023) showed the turbulent particle transport to largely dominate the NC transport and to exhibit a clear anti-gyro-Bohm scaling, this providing an efficient mechanism to explain the increased density gradient observed with increasing isotopic mass.

Regarding the dependence of the model predictions on the magnetic field, the gyro-Bohm normalisation $q_{e,gB}$ in the heat-flux scaling of (2.1) scales with B^2. Hence, as mentioned in § 3.2 above, the predicted T_e across the pedestal is expected to scale approximately with $B^{2/3}$. Hence, the higher toroidal field of the pulses considered here of 2.25 T compared with the 1.7 T of the pulses for which the q_e scaling was determined (Chapman-Oplopoiou *et al*. 2022), would result in a factor ∼1.52 increase in the predicted $T_{e,ped}$, provided other pulse parameters where held constant. The fact that at least the predicted T_e at the density pedestal top $T_e(\psi_N^{ne,top})$ agrees well with experiment, indicates that the electron heat flux, at least across the steep-density gradient region of the pedestal, likely does scale with the expected electron gyro-Bohm normalisation.

From the above, the key points are that the results presented here indicate:

(i) across the steep-density gradient region of the pedestal, the good agreement between the ETG model predictions and the measured profiles implies that the electron heat transport is probably predominately due to slab-ETG turbulence over this region, and is hence largely independent of A_{eff};

(ii) the reduction in $T_{e,ped}$ with A_{eff} is primarily due to the response of the n_e profile to changes in the particle transport with A_{eff};

(iii) the change with A_{eff} in the degree of agreement between the ETG model predictions and the measured profiles over the region of weak-density gradient inside the density pedestal top implies that the underlying scaling for the electron heat transport in this inner region of the pedestal must depend to some extent on A_{eff}.

5.3. *On the critical threshold for ETG turbulence*

Here, we discuss the conditions under which ETG-driven turbulence is expected to exhibit a threshold, normalised temperature gradient $R/L_{T_e,cr}$ or a threshold in the parameter η_e, the latter implying that an increased density gradient would require a larger temperature gradient to destabilise the turbulence. In which regions of the pedestal these different thresholds are expected to apply gives insight into their role in determining the pedestal structure.

For a study of the linear threshold temperature gradient for the destabilisation of ETG turbulence by Jenko *et al*. (2001), a series of linear stability calculations were performed using the GK code GENE, scanning a number of parameters over ranges representative of the core of a typical tokamak plasma equilibrium, to determine the scaling of the critical, normalised electron temperature gradient $R/L_{T_e,cr}$ required for finite growth rate of the most unstable linear mode, i.e. at which its growth rate $\gamma_m > 0$.

By separately fitting the scaling of $R/L_{T_e,cr}$ obtained for each parameter, e.g. the normalised density gradient R/L_{n_e}, the temperature ratio parameter $\tau = Z_{eff}(T_e/T_i)$, safety factor q, and the magnetic shear $\hat{s} = r/q(dq/dr)$, the overall scaling could be summarised by an expression of the form

$$R/L_{T_e,cr} = \{(1+\tau)(\mathcal{A} + \mathcal{B}\hat{s}/q), \mathcal{C}R/L_{n_e}\}_{max}, \tag{5.2}$$

where the fit coefficients are $\mathcal{A} = 1.33$ $\mathcal{B} = 1.91$, $\mathcal{C} = 0.8$ (see (4) of Jenko *et al*. (2001)). A more complete scaling, accounting for finite aspect ratio and non-circular plasma geometry is given by

$$R/L_{T_e,cr} = \{(1+\tau)(1.33 + 1.91\hat{s}/q)(1 - 1.5\epsilon)(1 + 0.3\epsilon(d\kappa/d\epsilon)), 0.8R/L_{n_e}\}_{max}, \tag{5.3}$$

where the inverse aspect ratio $\epsilon = r/R_0$ and $\kappa = b/a$ (where a and b are the horizontal and vertical plasma radii) is the elongation of the flux surfaces (see (7) of Jenko *et al*. (2001)).

The first and second terms in (5.2) and (5.3) represent the linear thresholds for what are known as the 'toroidal' and 'slab' branches of linear ETG modes, which we denote hereafter as T-ETG and S-ETG modes. For the slab modes, which dominate at high R/L_{n_e}, the parallel dynamics dominates over perpendicular drifts, while toroidal modes, which are driven by perpendicular drifts, are dominant at low R/L_{n_e} (Romanelli 1989; Jenko *et al*. 2001).

The behaviour of this threshold is made up of two parts, the constant $R/L_{T_e,cr}$ branch at low R/L_{n_e}, where the first term in (5.3) is largest and the branch at high R/L_{n_e} where $R/L_{T_e,cr} = 0.8R/L_{n_e}$. It is this second branch, corresponding to the dominance of S-ETG modes, that is appropriate at the high values of $R/L_{n_e} \sim \mathcal{O}(100)$ typical of the steep-density gradient region of the pedestal. With the

definition of the parameter $\eta_e = L_{n_e}/L_{T_e}$, this branch corresponds to the threshold $\eta_{e,cr} = 0.8$ for a finite linear growth rate of these modes.

The set of nonlinear, GENE simulations, over which the electron temperature and density gradients were scanned about nominal values of R/L_{T_e} and R/L_{n_e}, performed for the study of Chapman-Oplopoiou *et al*. (2022), were run only for the mid-pedestal location in the steep-density region. These showed that the ETG turbulence prevalent there exhibits a threshold in $\eta_{e,cr}$, with the threshold R/L_{T_e} increasing linearly with R/L_{n_e}, as expected for S-ETG modes. The saturated electron heat fluxes q_e from these simulations were found to decrease linearly with increasing R/L_{n_e} and increase with $(R/L_{T_e})^3$ for values well above threshold, these trends captured by the expression

$$Q_e^\star = (R/L_{n_e})^{-1}(R/L_{T_e} - R/L_{T_e,cr}) \equiv (\eta_e - \eta_{e,cr}). \tag{5.4}$$

Here, the dependence of the threshold η_e on the density gradient $\eta_{e,cr} = (R/L_{T_e,cr})(R/L_{n_e})$ is consistent with that found from the linear scans with GENE in Jenko *et al*. (2001), represented by the second term in (5.3).

Two expressions for the electron heat flux q_e were used in Chapman-Oplopoiou *et al*. (2022) to fit the data from the nonlinear GENE simulations from the temperature gradient scan, i.e. equation (i) $q_e \propto (\omega_{T_e} - \alpha\omega_{n_e,0})^\beta$ and equation (ii) $q_e \propto (\omega_{T_e} - \delta\omega_{n_e,0}))^\epsilon \omega_{T_e}^2$, where $\omega_{T_e} \equiv a/L_{T_e}$, etc. Only the latter equation (ii) can be transformed algebraically into (5.4). The fit found using equation (i) yielded a threshold $\alpha \equiv \eta_{e,cr} \sim 0.8$ and an exponent $\beta \sim 3$, while the fit using equation (ii) yielded a higher threshold $\delta \equiv \eta_{e,cr} \sim 1.28$ and an exponent $\epsilon \sim 1.43$.

It is interesting to note that fitting the q_e data using equation (i) yielded a threshold much closer to the linear threshold $\alpha \equiv \eta_{e,cr} \sim 0.8$, while the fitted exponent $\beta \sim 3$ is consistent with the prediction of critical balance theory for ETG turbulence (Barnes, Parra & Schekochihin 2011; Adkins *et al*. 2022, 2026), even for values of ω_{T_e} not far above threshold. In contrast, the higher threshold found by fitting to equation (ii) instead, results in a slightly stronger dependence of $q_e \propto (R/L_{T_e})^{3.4}$ only far above threshold. The similar uncertainties on the fit parameters found with either expression, meant that it was impossible to distinguish which of the two forms better fits the heat-flux data. It therefore remains an open question whether $\eta_{e,cr}$ lies at the linear threshold or whether there is an upward, nonlinear 'Dimits' shift to the threshold η_e for ETG turbulence in the pedestal region (Dimits *et al*. 2000).

The key points from the above discussion are:

(i) in regions with high $R/L_{T_e} \sim \mathcal{O}(100)$, as in the steep-density gradient region of the pedestal, the slab branch of ETG turbulence exhibits a threshold in η_e, hence, the threshold R/L_{T_e} is proportional to R/L_{n_e};

(ii) in contrast, where the density gradient is weak ($R/L_{T_e} < \mathcal{O}(10)$), as inside the density pedestal top, the toroidal branch of ETG turbulence is expected to prevail, which exhibits a threshold in R/L_{T_e} that is independent of R/L_{n_e};

(iii) above this critical threshold, the electron heat flux increases strongly $\propto (R/L_{T_e})^3$, implying that the ETG turbulence is critically balanced;

(iv) from the heat-flux scalings found compatible with the GK study of Chapman-Oplopoiou *et al*. (2022), it is not possible to ascertain whether or not the ETG turbulence in the steep-density gradient region exhibits a Dimits' shift in the critical η_e.

5.4. *On the structure of turbulence across the pedestal*

In the study of Chapman-Oplopoiou *et al*. (2022), the structure of turbulence across the pedestal of selected JET-Be/W type-I ELMy H-modes at 1.4 MA/1.7 T with varying input power and gas injection rates, from the weak-density region inside the pedestal top across the steep-density gradient region to the separatrix, is investigated in detail using both linear and nonlinear electromagnetic GK simulations using GENE. For the cases studied there, the heat flux was found to be carried predominantly by turbulent electron heat transport across most of the pedestal, except in one case for a pulse at lower heating power, in which neo-classical ion heat transport carried most of the heat flux across this region.

For the innermost flux surface considered, mid-way between the temperature and density pedestal top positions, the dominant modes were found to be ITG/TEM turbulence at low $k_y\rho_i$ and 'core-like' ETG turbulence (with growth rates peaking at the outboard mid-plane, i.e. $\theta_0 = 0$) at high $k_y\rho_i$. There, the electron heat-flux spectra were found to peak at larger scales, over the range of $k_y\rho_i \sim 10-20$, than in the steep-density gradient region.

At the mid-pedestal flux surface in the steep-density gradient region, the heat flux was found to be carried predominantly by S-ETG turbulence, the spectrally resolved electron heat flux peaking at $k_y\rho_i \sim 60$, i.e. where $k_y\rho_e \sim \mathcal{O}(1)$. Linearly, these modes were found to have a high parallel wavenumber k_z, indicating the importance of the parallel resonance ($\omega \sim k_z v_{th,e}$, where $v_{th,e}$ is the electron thermal velocity and k_z the wavenumber parallel to B) in their dynamics, thus confirming the S-ETG character of this turbulence.

A tendency for ETGs to exist also at smaller $k_y\rho_i$ in the steep-density gradient region was particularly noticeable for the high-power pulses. At $k_y\rho_i \lesssim 5$, the dominant form of ETG were found to be T-ETG modes, requiring large values of R/L_{T_e} to exist and with growth rates peaking at $\theta_0 \neq 0$, in contrast to the high k_z S-ETG modes present at high $k_y\rho_i$, which were found to carry the overwhelming fraction of the electron heat flux.

The cases studied with low gas fuelling rates also exhibited KBMs present close to the separatrix at $k_y\rho_i \sim 0.2$, characterised by their vanishing parallel electric field $E_\parallel$ and transport fingerprints, as described in Hatch *et al*. (2016) and Kotschenreuther *et al*. (2019).

Recently the GK study of JET-Be/W pedestal heat transport reported in Chapman-Oplopoiou *et al*. (2022) has been extended by performing a more detailed study of the morphology of the ETG turbulence reported in Chapman-Oplopoiou *et al*. (2025), with the aim of investigating why the cases with a higher gas fuelling rate exhibit a somewhat 'stiffer' $q_e(\eta_e)$ scaling than the low-gas cases. Here, the term 'stiffness' refers to the rate of increase of q_e with η_e, i.e. $\mathrm{d}q_e/\mathrm{d}\eta_e$. The relative importance of the toroidal and slab resonances could be investigated by comparing the resulting heat fluxes obtained from nonlinear GK simulations performed both with and without the toroidal drifts active. For the low-gas case, no difference was found between the cases with and without the toroidal drifts, indicating that the ETG turbulence is purely slab-like in character.

In contrast, for the high-gas case, which consequently has a higher ratio of separatrix to pedestal density $n_{e,sep}/n_{e,ped}$ (and hence lower normalised density gradient ω_{n_e} at the mid-pedestal flux surface) than the low-gas case, disabling the toroidal drifts significantly reduced the heat flux (by ~35 % at the nominal gradients), resulting in quantitatively very similar $q_e(\eta_e)$ scaling to the low-gas case. Hence, with a

weaker density gradient, an increasing relative contribution from T-ETG modes is found to be the underlying cause of the increased stiffness of the heat-flux scaling. As expected, the T-ETG modes were of a ballooning character, peaking at $k_z \sim 0$. Furthermore, it was found that, while variation of ω_{n_e} did not affect the $q_e(k_z)$ spectrum, increasing ω_{T_e} caused a pile up of the heat flux at high values of k_z at the limit of the parallel resolution of the GK simulations, as is also documented for S-ETG modes in Pueschel *et al*. (2019).

In the detailed GK study of Parisi *et al*. (2020) of the pedestal of the 1.4 MA/1.9 T JET-Be/W pulse no. 92174 with 17.4 MW of heating power, the turbulence for a flux surface in the steep-density gradient region was found to be dominated by ETG turbulence for all $k_y\rho_i > 0.1$, with a novel type of T-ETG instability found often to be the fastest growing mode for $k_y\rho_i \geqslant 1$. These modes exhibited such large radial wavenumbers for electron Larmor radius effects to be important, i.e. $k_x\rho_e \sim 1$. This mode was found to be driven far away from the outboard mid-plane, i.e. $\theta_0 \neq 0$, and to exist at large spatial scales, where $k_y\rho_i \sim (\rho_i/\rho_e)(L_{T_e}/R) \sim 1$, which is consistent with the results reported in Told *et al*. (2008).

The T-ETG modes were found to co-exist with S-ETG modes, with the latter dominant at $\theta_0 = 0$ for $k_y\rho_i \geqslant 5$. Quasi-linear, mixing-length arguments indicated that both the T-ETG and S-ETG modes were expected to make comparable contributions to the electron heat transport. While growth rates of the S-ETG modes were found to decrease with R/L_{n_e}, the T-ETG modes were insensitive to R/L_{n_e} but strongly driven by R/L_{T_e}. At all scales, ITG modes were found to be subdominant and KBMs were shown to be suppressed by $E\times B$ shear.

In another recent study by Leppin *et al*. (2023), the structure of turbulence across a typical pedestal in ASDEX Upgrade was determined using a combination of linear and nonlinear, global electromagnetic GK simulations performed using GENE. Trapped-electron-driven mode (TEM) turbulence with electromagnetic components due to MTMs was found to be dominant at the pedestal top/shoulder, while a combination of linear stabilisation and $E\times B$ shear was found to suppress such ion-scale turbulence towards the steep gradient region, where the electron heat flux was instead carried by small-scale ETG modes and the ion channel reduced to neo-classical levels.

Of particular relevance to this present work is the finding of each of the studies discussed above that small-scale ETG turbulence carries the dominant fraction of the electron heat flux across the steep-density region of the pedestal. This turbulence has a predominantly 'slab' structure, with high parallel wavenumber k_z and a threshold in η_e close to or somewhat above the linear threshold, although there is an increase in the relative contribution from T-ETG modes, driven by toroidal drifts, as the density gradient weakens. Furthermore, across the weak-density gradient region inwards of the density pedestal top, other larger-scale ITG/TEM modes or electromagnetic MTMs are found to carry a significant fraction of the electron heat flux.

It is across this inner region of the pedestal that the model for the temperature profile of § 2 breaks down, as here the heat-flux scaling for the steep-density gradient region on which it is based is invalid. Further sets of nonlinear GK calculations scanning the temperature and density gradients are required to determine the appropriate electron heat-flux scaling to adopt for this region, which would have to be global to capture the ion-scale modes. Furthermore, in order to accurately determine the scaling, it may also be necessary to perform multi-scale GK simulations to capture any effects of cross-scale coupling between electron- and ion-scale turbulence (Howard *et al*. 2015; Pueschel *et al*. 2020). Ideally, other parameters as appear in (5.3) for

the threshold R/L_{T_e}, e.g. $\hat{s}/q$ should also be scanned to further parameterise the heat-flux scaling. Note that estimates of the magnitude of $R/L_{T_{e,cr}}$ obtained from the first term of (5.3) using typical values of the parameters for the region at the pedestal top give too low values for $R/L_{T_{e,cr}}$ of $\mathcal{O}(1)$ compared with the observed values which are of $\mathcal{O}(10)$ in this inner region of the pedestal.

6. Predictions using the EPED model combined with the ETG critical-heat-flux model

The EPED model of Snyder *et al*. (2009) for prediction of the total pressure at the pedestal top p_{ped} is based on two assumptions: (i) that the pressure pedestal width Δ_p is determined by the stability of KBMs, which limit the pressure gradient p'_{tot} across the pedestal, yielding the relation $\Delta_p = 0.076\,\beta_{p,ped}^{1/2}$;[2] and (ii) the pedestal height is determined by increasing p_{ped} until the magneto-hydro-dynamic (MHD) stability limit set by peeling-ballooning instabilities (Snyder *et al*. 2002) is reached, above which an ELM would be triggered. Hence, in order to determine $T_{e,ped}$, using the EPED model it is necessary to assume a prescribed pedestal density $n_{e,ped}$.

Typically, equal electron and ion temperatures ($T_e = T_i$) and equal widths for the electron density, temperature and pressure pedestals ($\Delta_{n_e} = \Delta_{T_e} = \Delta_p$) are assumed. As an attempt to improve upon this aspect of the EPED model, we have incorporated the ETG critical-heat-flux model of Field *et al*. (2023) for the pedestal T_e profile into a modified version of EPED in two different ways, as described in § 6.1 below. As a further step, the ionisation/diffusion model of Saarelma *et al*. (2023) has also been used to predict the pedestal n_e profile. This, in combination with the EPED prediction of the total pedestal pressure p_{ped}, also allows the pedestal T_i profile to be determined. Results from applying these models to the JET-Be/W isotope mass scan dataset (Frassinetti *et al*. 2023) are presented in the following § 6.2.

6.1. *Combined EPED and ETG critical-heat-flux pedestal models*

The standard EPED model of Snyder *et al*. (2009) for prediction of the total pedestal pressure p_{ped} functions in the following way: a range of pedestal widths Δ_p are assumed from which profiles of the total pedestal pressure p_{ped} are constructed using the relation $p_{ped} \propto \Delta_p^2$, which derives from the KBM pressure-gradient constraint $\Delta_p = 0.076\,\beta_p^{1/2}$; two-dimensional equilibria, constructed for each pressure profile, are tested for MHD stability to peeling-ballooning modes (PBM) using the MISHKA code (Mikhailovskii *et al*. 1997) and that which is marginally stable then gives the EPED prediction of p_{ped}. The marginal stability criterion on the growth rate γ used here is $\gamma > \omega^\star_{p_i}/2$, where $\omega^\star_{p_i}$ is the ion diamagnetic frequency.

The ETG critical-heat-flux model for the pedestal T_e profile of Field *et al*. (2023), allows calculation of the T_e profile across the pedestal, given the n_e profile and the heat flux across the pedestal P_{sep}/S as input. This model has been combined with the standard EPED model within Europed in various ways, forming the models M1–3 described below.

The first two models still take $n_{e,ped}$ as an input and use the ETG model to calculate the associated T_e profile. A consequence of this is that the resulting $T_{e,ped}$ is extremely sensitive to the ratio $n_{e,sep}/n_{e,ped}$, increasing values of this density ratio

[2]The pedestal poloidal beta β_p is the total pedestal pressure p_{ped} normalised to the energy density of the poloidal magnetic field, defined as: $\beta_{p,ped} = p_{ped}/(2\mu_0 \bar{B}_p^2)$, where $\bar{B}_p$ is the flux-surface-averaged poloidal magnetic field.

causing $T_{e,ped}$ to decrease strongly. This sensitivity causes the first model (M1), which does not use the KBM constraint to determine the total pressure p_{ped}, to fail in some cases at the experimental value of this density ratio.

For the second model (M2), the ETG model is combined with EPED, where the T_e profile from the ETG model is used together with the EPED prediction of the total pressure p_{tot} and pedestal width Δ_p to determine the T_i profile.

The third model (M3) combines the ETG critical-heat-flux model for the pedestal T_e profile with the density-prediction (DP) model of Saarelma *et al*. (2023), a brief description of which is given in Appendix B. An iterative process is used, where the predicted n_e profile is used as an input to the ETG model to predict the T_e profile, which is then fed back into the DP model, resulting in a self-consistent prediction of the n_e and T_e profiles. By combining this model with the MHD and KBM constraints of the EPED model the T_i profile can also be predicted, thereby providing a complete prediction of the pedestal profiles.

An algorithmic style description of the three models M1-3 follows:

M1: with $n_{e,ped}$ given, assuming $T_i/T_e = const$ but without the EPED KBM constraint:

(i) a range of pedestal widths Δ_p are generated, which together with the experimental value of $n_{e,ped}$, gives a range of pedestal n_e profiles;

(ii) for each of these n_e profiles a corresponding T_e profile is calculated using the ETG critical-heat-flux model, as explained in § 3 of Field *et al*. (2023);

(iii) the total pressure $p_{tot} = p_i + p_e$ is calculated, assuming a fixed ratio of $T_i/T_e = const$ and taking account of ion dilution using the measured Z_{eff} and a representative impurity charge state Z_I;

(iv) the resulting p_{tot} profiles are used to generate a range of self-consistent equilibria, each of which are tested for stability to ideal MHD PBM using the MISHKA code;

(v) the profile which is found to be marginally stable then yields a prediction of p_{tot} and the corresponding $n_{e,ped}$ and $T_{e,ped}$.

M2: with $n_{e,ped}$ given, determine: p_{tot} from EPED, T_e from ETG model and T_i by matching p_{tot} from the EPED KBM and MHD (PBM) constraints:

(i) a range of pedestal widths Δ_p are generated and for each the given value of $n_{e,ped}$, gives a range of pedestal n_e profiles;

(ii) for each of these n_e profiles the corresponding T_e profile is calculated using the ETG critical-heat-flux model, as explained in § 3 of Field *et al*. (2023);

(iii) for each Δ_p the corresponding p_{tot} profile is calculated using the KBM constraint, i.e. $p_{ped} \propto \Delta_p^2$;

(iv) the resulting p_{tot} profiles are used to generate a range of self-consistent equilibria, each of which are tested for stability to ideal MHD PBM using the MISHKA code;

(v) the profile which is found to be marginally stable then yields a prediction of p_{tot} and the corresponding $n_{e,ped}$ and $T_{e,ped}$;

(vi) to satisfy the KBM constraint, the T_i profile is determined from p_{tot}, i.e. $T_i = (p_{tot} - p_e))/n_i$.

M3: the density pedestal prediction model of Saarelma *et al*. (2023) combined with the ETG critical-heat-flux model and the EPED KBM constraint ($\Delta = 0.076\sqrt{\beta_{p,ped}}$):

(i) an initial guess is made of $n_{e,ped}$ and $T_{e,ped}$;

(ii) a range of pedestal widths Δ_p are generated and for each width corresponding n_e and T_e profiles are generated;

(iii) for each width Δ_p the condition $\Delta_p = 0.076\,\beta_{p,ped}^{1/2}$ is used to solve first $\beta_{p,ped}$ and then for p_{ped} from $\beta_{p,ped}$;

(iv) $T_{i,ped}$ is solved from $p_{ped} = p_{e,ped} + p_{i,ped}$, where $p_{i,ped} = n_{e,ped}(T_{e,ped} + T_{i,ped}((1 + Z_I - Z_{eff}))/Z_I)$ and Z_I is the charge state of a representative low-Z impurity, e.g. Be^{+4};

(v) for each width Δ_p, the initial n_e, T_e and T_i profiles are input to the DP model (along with the other model parameters, described below) to predict the corresponding n_e profile;

(vi) the resulting n_e profile is then input to the ETG model to predict the corresponding T_e profile;

(vii) steps (iv) and (v) are iterated until the resulting n_e and T_e profiles converge;

(viii) steps (iii) to (v) are iterated until the resulting T_i profile converges;

(ix) for each of the cases corresponding to the different pedestal widths Δ_p, the total pressure profile $p_{tot} = p_e + p_i$ is calculated;

(x) the resulting p_{tot} profiles are used to generate a range of self-consistent equilibria, each of which are tested for stability to ideal MHD PBM using the MISHKA code;

(xi) the p_{tot} profile which is found to be marginally stable then yields a prediction of the pedestal n_e, T_e and T_i profiles;

(xii) after fitting the predicted profiles with model mtanh() functions, the corresponding values of $n_{e,ped}$, $T_{e,ped}$ and $T_{i,ped}$ are obtained.

The principal inputs to model M3, which provides a full prediction of the pedestal profiles, are:

(i) the experimental input parameters: i.e. the heat flux across the separatrix P_{sep}/S and the electron density $n_{e,sep}$ and temperature $T_{e,sep}$ at the separatrix;

(ii) several, less accurately known 'model' parameters of the DP model, to which the $n_{e,ped}$ predictions are less sensitive: the flux-surface-averaged (FSA) density of Franck–Condon neutral atoms at the separatrix $\langle n_{FC}(0)\rangle$; the assumed ratio of electron particle diffusivity to electron heat conductivity $((D_e/\chi_e)_{TG}$ across the pedestal due to temperature-gradient-driven (ITG and ETG) turbulence; and the ratio of charge-exchange to Franck–Condon neutral densities at the separatrix $(n_{CX}/n_{FC})|_{x=0}$.

(iii) For the ETG critical-heat-flux model, there are also the model parameters of (α, β and $\eta_{e,cr}$) of the underlying gyro-Bohm normalised electron heat-flux scaling (2.1).

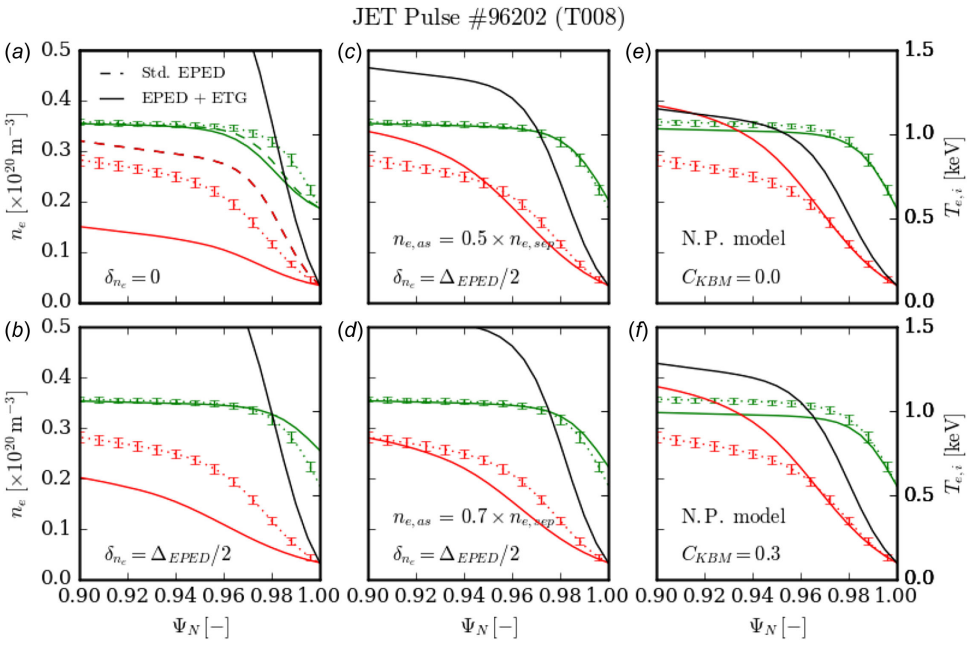

FIGURE 5. *Pedestal profiles for the D pulse no. 96202 at the low fuelling rate of* $\Gamma_{gas} \sim 0.74 \times 10^{22}$ es^{-1} *showing* n_e *(green),* T_e *(red) and* T_i *(black) vs normalised poloidal flux* ψ_N *from various EPED based models. Experimental profile fits are shown by the 'dotted' lines with the error bars. Profiles are shown in (a) calculated using standard EPED ('dashed' lines) and from the combined ETG + EPED model (M2) ('solid' lines). In (b–d) the* n_e *profile is shifted outwards by* $\delta_n = \Delta_p/2$*, with* T_e *calculated using the ETG model; in (c) the* n_e *profile asymptotes to* $0.5 \times n_{e,sep}$ *outside the separatrix; in (d) the* n_e *profile asymptotes instead to* $0.7 \times n_{e,sep}$*. In (e, f), the* n_e *profile is calculated using the DP model of* Saarelma *et al.* (2023)*, the* T_e *profile is calculated using the ETG model and* T_i *is determined for consistency with the EPED prediction of* p_{tot}*; in (e) with coefficient* $C_{KBM} = 0$ *and in (d) with* $C_{KBM} = 0.3$.

A discussion of the sensitivities of the predictions of the combined ETG+EPED+DP model (M3) to these experimental input and model parameters is given in Appendix C.

6.2. *Results of applying combined EPED + ETG pedestal models to isotope scan pulses*

M1: the strong inverse dependence of the value of $T_{e,ped}$ predicted using the ETG model on the density ratio $n_{e,sep}/n_{e,ped}$, which is a result of the stiffness of the ETG heat-flux clamping η_e to values not far above $\eta_{e,cr}$ as discussed in Field *et al.* (2023), causes the model to fail, i.e. never reaching marginal MHD stability, for some cases with higher values of this ratio. For this reason, this model, which does not use the EPED KBM constraint, has not been explored further.

M2: results from applying model M2 to one of the pulses from the isotope mass scan dataset discussed here (no. 96202), at a low gas fuelling rate of $\Gamma_{gas} \sim 0.74 \times 10^{22}$ es^{-1}, are shown in figure 5(*a–d*). Both the predicted T_e profile from the standard EPED and from the combined model M2 are shown for four different density profiles with the same $n_{e,ped}$, which explore the dependence of the predicted $T_{e,ped}$ on the density ratio $n_{e,sep}/n_{e,ped}$.

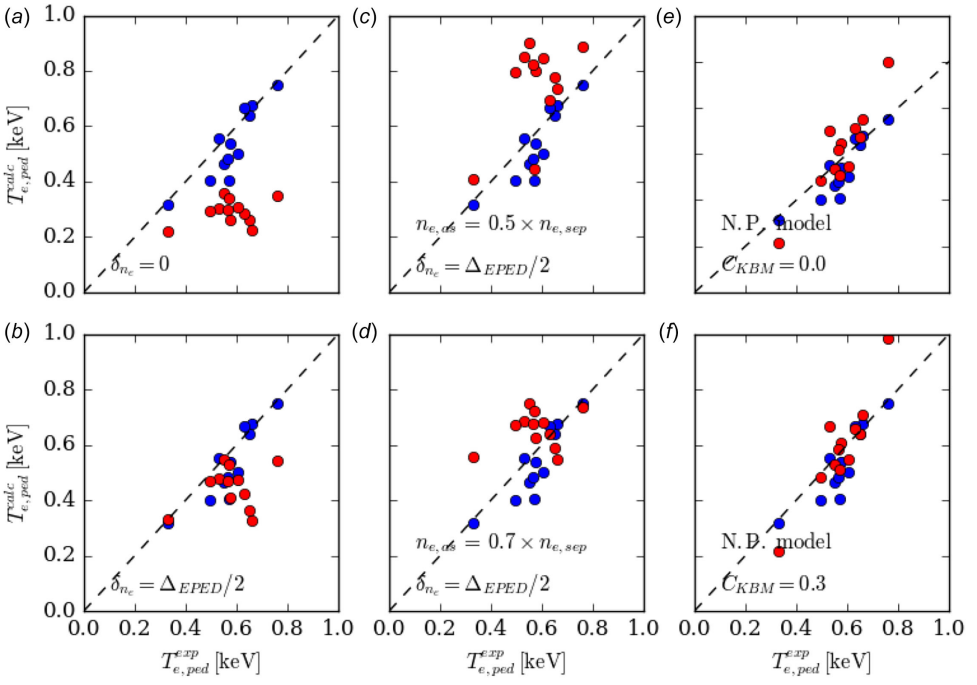

FIGURE 6. *Predicted values of the pedestal electron temperature $T^{calc}_{e,ped}$ vs experimental values $T^{exp}_{e,ped}$, with $T^{calc}_{e,ped}$ calculated using the standard EPED model (•) and from each of the various EPED based pedestal models (•) corresponding to the same model cases as in figure 5 (a–f) above, each for all of the* 2.0 MA *pulses from the isotope mass and fuelling rate scans in table 1.*

For the first case (*a*) following the standard EPED, the n_e profile position is at $\Delta_{n_e}/2$ inside the separatrix and the profile asymptotes to the experimental $n_{e,sep}$ outside the separatrix. This results in too low a predicted T_e from the ETG model, which is has to be compensated by too high values of T_i required to match the predicted p_{tot} from EPED. Note that for the pulses in the dataset discussed here, the experimental values of $T_i \sim T_e$ in the pedestal region, although relatively large uncertainties preclude a detailed comparison with our predictions.

For the other cases (*b–c*), the n_e profiles are shifted outwards by $\Delta_{n_e}/2$ from the standard EFIT case (*a*), i.e. the centre position is located at the separatrix. In case (*b*), this shift increases the ratio $n_{e,sep}/n_{e,ped}$, resulting in similarly too low values of T_e and too high values of T_i, as for case (*a*). In case (*c* and *d*), the asymptotic value of n_e outside the separatrix is reduced to $0.5 \times n_{e,sep}$ and $0.7 \times n_{e,sep}$, respectively. For the lowest resulting ratio $n_{e,sep}/n_{e,ped}$ of case (*c*), the predicted T_e profile is the closest to the experimental profile and the predicted T_i profile closest to T_e, although still considerably higher.

Results from applying model M2 to the full isotope mass scan dataset are shown in figures 6, 7 and 8, which compare the calculated $T_{e,ped}$, $n_{e,ped}$ and Δ_p from the standard EPED and from the various combined models with the experimental values, respectively. The most accurate predictions of $T_{e,ped}$ are for case (*d*). However, for this case, the predicted pedestal widths Δ_p are wider than the experimental values.

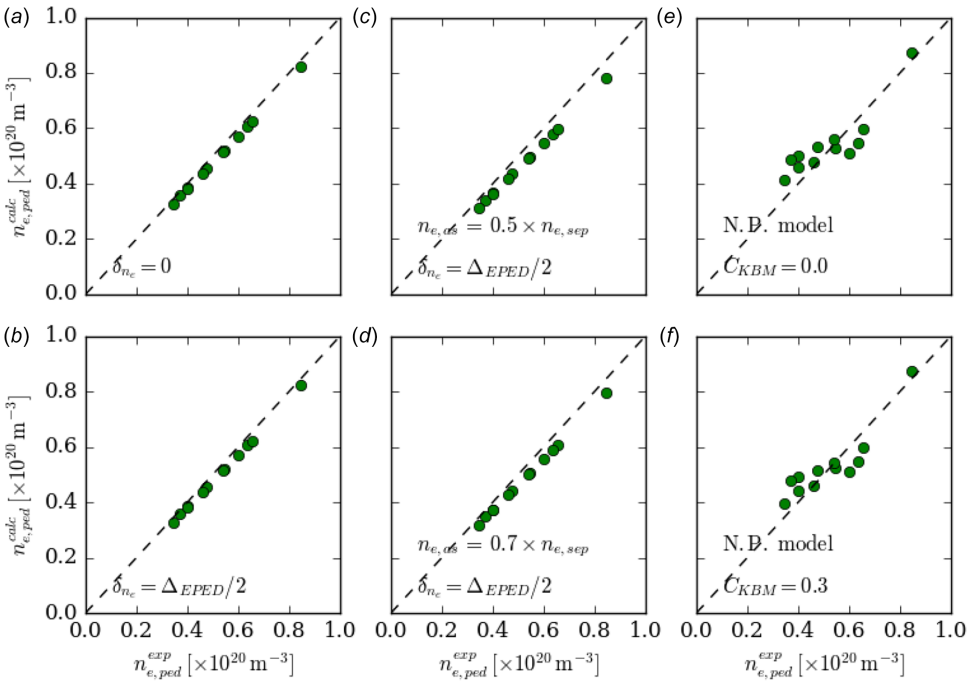

FIGURE 7. *Predicted values of the pedestal density* $n^{calc}_{e,ped}$ *vs experimental values* $n^{exp}_{e,ped}$ *from each of the various EPED based pedestal models* (•) *corresponding to the same model cases as in figure 5(a–f) above, each for all of the* 2.0 MA *pulses from the isotope mass and fuelling rate scans in table 1.*

For these pulses, the standard EPED predicts quite constant values of Δ_p, which are mostly narrower than the experimental widths. Note that the values of $n_{e,ped}$ shown in figure 7(*a–d*) from model M2, which takes $n_{e,ped}$ as an input, differ slightly from the experimental values because the former are obtained from a fit to the analytic model profile rather than from a fit to the experimental data.

For all of the cases modelled here, we do not take into account the variation of $(D_e/\chi_e)_{TG}$ with A_{eff}. A value of the heat-to-particle diffusivity ratio $(D_e/\chi_e)_{TG} = 0.3\dot{3}$ is assumed in the DP model, which is appropriate for the mid-range value $A_{eff} = 2.5$ over the D:T isotope-mix scan. Results of GK simulations reported in Predebon *et al*. (2023) for JET-Be/W pulses with different values of A_{eff}, found values of $(D_e/\chi_e)_{TG}$ of $0.5 \rightarrow 0.25$ over the range of $A_{eff} = 2 \rightarrow 3$, i.e. a decreasing relative level of particle to heat transport with increasing A_{eff}. As discussed in Appendix C below, the sensitivity of the calculated $n_{e,ped}$ from the DP model prediction to $(D_e/\chi_e)_{TG}$ is quite weak. For an example JET-Be/W case (no. 96201), doubling $(D_e/\chi_e)_{TG}$ from $0.25 \rightarrow 0.5$ is found to decrease the predicted $n_{e,ped}$ by only $\sim$12 %.
M3: results from applying model M3, which combines the density pedestal prediction model of Saarelma *et al*. (2023), the ETG critical-heat-flux model and the EPED KBM constraint, to profiles from the D pulse no. 96202 are shown in plots (*e*, *f*) of figure 5 and to the full dataset of pulses in table 1 in plots (*e*, *f*) of figures 6, 7 and 8.

The difference between the two cases is the value of the KBM coefficient C_{KBM}, which is set to 0 and 0.3 for plots (*e*) and (*f*), respectively. This coefficient

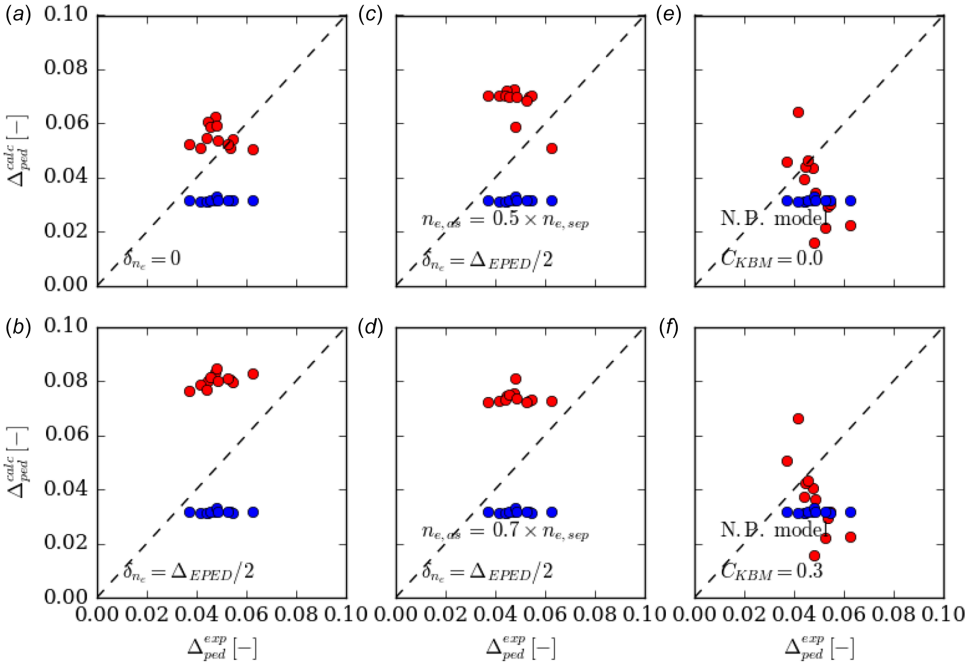

FIGURE 8. *Predicted values of the pedestal width Δ_p^{calc} vs experimental values Δ_p^{exp}, with Δ_p^{calc} calculated using the standard EPED (•) model and from each of the various EPED based pedestal models (•) corresponding to the same model cases as in figure 5 (a–f) above, each for all of the* 2.0 MA *pulses from the isotope mass and fuelling rate scans in table 1.*

is a multiplier on the contribution to the particle diffusivity from KBM modes ($D_{KBM} = C_{KBM}(\alpha - \alpha_{cr}), \alpha > \alpha_{cr}$). Hence, for $C_{KBM} > 0$, KBM modes can contribute to particle transport if $\alpha > \alpha_{cr}$ but not if $C_{KBM} = 0$. The similarity between the results shown for these two cases show that KBM modes are not predicted to contribute significantly to particle transport across the pedestal for these cases.

The overall agreement between the predicted pedestal T_e profiles from model M3 and the experimental profiles is the best of those from the three combined models, with a slight improvement over the standard EPED predictions. Both the predicted $n_{e,ped}$ and $T_{e,ped}$ generally agree well (within $\sim \pm$ %10) with the experimental values.

Although both the predicted $n_{e,ped}$ and $T_{e,ped}$ increase with the experimental values, the predicted values of $T_{e,ped}$ tend to increase faster than linearly, while the predicted $n_{e,ped}$, increase more slowly. Including the dependence of $(D_e/\chi_e)_{TG}$ on A_{eff} rather than assuming the constant value of $0.3\dot{3}$ would likely improve the degree of agreement between the calculated and experimental values of $n_{e,ped}$.

The predicted pedestal widths Δ_p are of approximately the correct magnitude, however, these exhibit an opposite trend to the experimental values, i.e. smaller widths are predicted for wider experimental pedestals.

7. Conclusions

The fact that the model described in § 2 for the pedestal electron temperature profile is able to predict the electron temperature at the top of the density pedestal $T_e(\psi_N^{n_{e,top}})$ with reasonable veracity across these scans of effective isotope mass A_{eff}

and gas fuelling rate, supports the underlying assumption of the model that the electron heat transport across this region of the pedestal is dominated by turbulent heat transport due to ETG modes. The S-ETG turbulence prevailing in a regime with a strong density gradient exhibits a critical threshold in the parameter η_e, rather than of R/L_{n_e}, which results in the T_e profile being intimately related to the n_e profile.

Currently, the model is based on the simple scaling of the gyro-Bohm normalised electron heat flux of (2.1) with η_e alone. As the electron gyro-Bohm normalisation depends only on the local T_e gradient scale length L_{T_e}, the magnetic field B and the electron mass m_e, this scaling is independent of the ion mass and hence exhibits no dependence on A_{eff}. The agreement of the predicted T_e at the top of the density pedestal $T_e(\psi_N^{n_{e,top}})$ across the effective isotopic mass A_{eff} scan data set results purely as a consequence of the electron heat transport responding to changes to the density profile occurring with the change in A_{eff}, which can affect the relative level of electron particle compared with heat transport, e.g. as has been found in the recent study of Predebon *et al*. (2023).

As can be seen e.g. from figure 1(*d*), the adopted electron heat flux-scaling tends to over-/under-predict R/L_{T_e} outside/inside the mid-pedestal location for which the scaling was derived. Although these effects largely compensate, resulting in a reasonable prediction of $T_e(\psi_N^{n_{e,top}})$, this indicates that this scaling is probably over simplified. It is likely that other parameters are also relevant in controlling the electron heat transport, e.g. the magnetic shear $\hat{s}$, which increases strongly towards the separatrix.

The value of $T_{e,ped}$, which is determined from the mtanh() fit to the T_e profile, is always higher than that at the density pedestal top $T_e(\psi_N^{n_{e,top}})$, which in turn is a consequence of the inward shift of the pedestal T_e profile with respect to the n_e profile. This shift is actually a consequence of the underlying turbulent electron heat transport requiring that η_e exceed a value $\mathcal{O}(2)$ to be able to carry the imposed heat flux q_e across the pedestal. Note that for $\eta_e = 1$, the profiles of R/L_{T_e} and R/L_{n_e} are identical and there is no relative shift between the T_e and n_e profiles, while for $\eta_e > 1$ the resulting T_e profile is shifted inwards with respect to the n_e profile and *vice versa*.

The higher values of $T_{e,ped}$ than $T_e(\psi_N^{n_{e,top}})$ are a consequence of T_e continuing to increase across the weak-density gradient region inside the density pedestal top. In this region, the assumed heat-flux scaling of (2.1) is invalid, resulting in an under-prediction of R/L_{T_e}, i.e. an over-prediction of the resulting electron heat flux. The findings of several of the pedestal GK studies discussed in § 5 that other modes than S-ETG modes are dominant in this region, implies that the electron heat transport is unlikely to be governed by η_e. This hypothesis is consistent with the expression proposed in Jenko *et al*. (2001) for the critical threshold for ETG turbulence, which implies that $R/L_{T_{e,cr}}$ is independent of R/L_{n_e} when the density gradient is weak.

The critical role of the pedestal density profile in largely determining the electron temperature profile, means that in order to be able to predict $T_{e,ped}$, any stand-alone model for the T_e profile must also incorporate a model for the density profile. A recent model for the pedestal density profile by Saarelma *et al*. (2023), which is a refinement of the ionisation/diffusion model of Groebner *et al*. (2002), extended to include a self-consistent population of charge-exchange neutral atoms.

This model has been tested against the EUROFusion Pedestal Database (Frassinetti *et al*. 2021) and is found, in particular, to be able to reproduce the observed increase in $n_{e,ped}$ with isotope mass A_{eff}. This arises primarily from the

strong sensitivity of the predicted $n_{e,ped}$ to the assumed value of $n_{e,sep}$, which is an input to the model, the former increasing with the latter. However, to reproduce the observations accurately, it was also necessary to adjust the assumed ratio of electron particle diffusivity to electron heat conductivity (D_e/χ_e), by decreasing this ratio with increasing A_{eff} (from 1 in H to 0.5 in D and 0.25 in T) (Saarelma *et al*. 2023), broadly consistent with the trends found in the study of Predebon *et al*. (2023).

Hence, the boundary conditions at the separatrix, $T_{e,sep}$ and in particular $n_{e,sep}$, are critical for determining both the electron density and temperature profiles across the pedestal, which are determined by heat and particle transport in the SOL, rather than details of transport processes within the confined plasma. The main control parameters determining $T_{e,sep}$ and $n_{e,sep}$ are the heat and particle fluxes into the SOL, although these also depend on the geometry of the SOL, i.e. the plasma shape and on the divertor configuration. Hence, as is well appreciated by machine operators, the plasma heating and fuelling are the principal means for influencing the pedestal parameters.

Three different numerical pedestal models, combining EPED with the ETG heat-flux model of Field *et al*. (2023) discussed here, have been tested against the isotope and fuelling rate scan dataset discussed here. The first two models take $n_{e,ped}$ as an input, while the third combines EPED, the ETG heat-flux model and the DP model of Saarelma *et al*. (2023). The first model, which does not use the EPED KBM constraint, fails on many cases due to the strong dependence of the predicted $T_{e,ped}$ from the ETG model on $n_{e,sep}/n_{e,ped}$. The second model, which uses the KBM constraint ($p_{tot} \propto \Delta_p^2$), provides predictions of both the T_e profile from the ETG model and the T_i profile by matching the total pressure p_{tot}. The third model, which provides a full prediction of the pedestal profiles, exhibits a reasonable agreement between the model predictions and experiment, implying that this model encapsulates the main physics underlying the pedestal structure.

It is illuminating to determine the scaling of $n_{e,sep}$ with the power crossing the separatrix in the electron channel $P_{e,sep}$ and the electron particle fuelling rate into the SOL Γ_e for the admittedly grossly over simplified case of a a collisionless SOL, which is sheath limited at the divertor target. This can be derived from the simple two-point model of Stangeby (2000), as described in Appendix B, which predicts that $n_{e,sep}$ should increase with isotope mass $\propto A_{eff}^{1/2}$ and also with the particle fuelling rate into the SOL $\propto \Gamma_e^{3/2}$ and decrease with the loss power across the separatrix $\propto P_{sep}^{-1/2}$.

Note that an extension of this 2-point model to incorporate the temperature dependence of the parallel electron heat conductivity $\kappa_\parallel \propto T_e^{5/2}$ predicts a very weak power scaling for $T_{e,sep} \propto P_{sep}^{2/7}$. Hence, the influence of the loss power on the pedestal due to changes to the separatrix boundary conditions is stronger through its effect on $n_{e,sep}$ than through its effect on $T_{e,sep}$. Note that modelling of JET-Be/W plasmas with neon impurity seeding described in Simpson *et al*. (2019) demonstrated agreement between the scaling $T_{e,sep} \propto P_{sep}^{2/7}$ with the results of simulations using the EDGE2D-EIRENE code (Reiter *et al*. 1995), provided the dependence of λ_q, the characteristic decay length of the parallel heat flux across the SOL, on the density and radiation in the SOL was taken into account.

This over-simplified scaling would predict an increase in $n_{e,sep}$ by a factor $\sim$1.2 changing isotope alone from D to T, which is less than the observed increase of a factor $\sim$1.6 at constant Γ_{gas} as shown in figure 2(*b*). However, this 'toy' model does illustrate how SOL physics can influence the boundary conditions at the separatrix and hence indirectly govern the pedestal structure. Of course, realistic simulations require much more complex two-dimensional models, such as the coupled fluid and

Monte Carlo neutrals simulation code EDGE2D-EIRENE (Reiter *et al*. 1995), to account for the complex processes occurring in a high-density, recycling SOL and particularly with a detached divertor where impurity and molecular radiation and charge-exchange heat and momentum losses play a dominant role.

Acknowledgements

This work has been carried out within the framework of the EUROfusion Consortium, funded by the European Union via the Euratom Research and Training Programme (Grant Agreement No. 101052200 – EUROfusion) and from the EPSRC (grant number EP/W006839/1). The data that support the findings of this study are openly available in the Open Data Register at https://doi.org/10.14468/tcey-2p41, reference number 2026-03-03-14-04-44-640878. To obtain further information on the data and models underlying this paper please contact PublicationsManager@ukaea.uk. Views and opinions expressed are, however, those of the author(s) only and do not necessarily reflect those of the European Union or the European Commission. Neither the European Union nor the European Commission can be held responsible for them.

Editor Eleonora Viezzer thanks the referees for their advice in evaluating this article.

Declaration of interests

The authors report no conflicts of interest.

Appendix A. Parameters of JET-Be/W experimental cases

See table 1.

Pulse no.	**PPF** no.	$\boldsymbol{t_0 - t_1}$ [s]	$\boldsymbol{A_{eff}}$ [–]	$\boldsymbol{\Gamma_{gas}}$ [10^{22} es^{-1}]	$\boldsymbol{P_{abs}}$ [MW]	$\boldsymbol{P_{Rad}^{iELM}}$ [MW]	$\boldsymbol{\langle P_{ELM}\rangle}$ [MW]	$\boldsymbol{P_{sep}^{iELM}}$ [MW]	$\boldsymbol{f_{ELM}}$ [Hz]
96201	T008	51.4–52.1	2.0	2.7	18.2	2.6	**9.1**	**6.5**	**72**
96202	T008	52.4–54.1	2.0	0.73	14.2	3.7	4.5	5.0	39
96208	T058	51.6–52.8	2.0	1.7	17.3	2.8	**6.9**	**7.6**	**83**
99480	T003	48.0–49.4	2.6	1.8	15.7	2.5	6.2	6.9	54
99490a	T005	48.3–49.7	2.7	1.6	15.6	6.2	2.7	6.7	27
99490b	T007	50.1–51.3	2.6	1.6	14.8	4.2	4.7	5.9	54
99491a	T003	48.3–49.4	2.4	1.5	16.3	5.2	4.2	6.9	40
99491b	T005	50.1–51.8	2.5	1.5	14.9	3.6	**6.5**	**4.8**	**72**
100247a	T003	47.8–49.1	3.0	1.7	12.6	4.8	1.9	5.8	18
100247b	T004	49.7–50.9	3.0	1.8	12.7	5.9	1.5	5.4	32
100183	T003	48.4–49.5	3.0	3.0	12.4	7.0	0.5	4.9	7.5
100185	T004	47.6–48.0	3.0	1.1	11.5	2.9	3.7	4.9	43

TABLE 1. *Parameters of the* 2.0 MA *JET-Be/W H-mode pulses and the corresponding fitted pedestal profile data files (PPFs): pulse number, PPF number, averaging time period* $t_0 - t_1$, *effective isotope mass* A_{eff}, *gas fuelling rate* Γ_{gas}, *absorbed heating power* P_{abs}, *radiated power from confined plasma* P_{Rad}^{iELM}, *time-averaged ELM loss power* $\langle P_{ELM}\rangle$, *averaged conducted power across the pedestal between ELMs* P_{sep}^{iELM} *and average ELM frequency* f_{ELM}. *Note that for some pulses the multiple PPFs correspond to different time periods during the pulse. Cases for which the ELM frequency is particularly high* ($f_{ELM} > 70$ Hz), *for which values of* P_{sep}^{iELM} *are likely to be more uncertain, are in bold font.*

Appendix B. Physics basis of the combined ETG+DP pedestal model (M3)

The predictive density pedestal model of Saarelma *et al*. (2023, 2024) is based on an analytic model of neutral penetration combined with a model for diffusive pedestal transport. The neutral-penetration model is an extension of the model of Groebner *et al*. (2003) to include the ionisation source of hot, charge-exchange hydrogenic neutral atoms, as well as that of lower energy, Franck–Condon atoms from molecular dissociation. A diffusion model for the charge-exchange neutral penetration becomes valid when $\sigma_{CX} v_{th,i} \gg \sigma_i v_{th,e}$ (where σ_{CX} and σ_i are the charge-exchange and ionisation cross-sections, respectively, and $v_{th,i}$ and $v_{th,e}$ are the ion and electron thermal velocities), which is appropriate for higher pedestal temperatures $\gtrsim \mathcal{O}(1\,\mathrm{keV})$.

In this model, the radial profile of the electron density $n_e(r)$ in the pedestal region is calculated by balancing radial particle diffusion, with coefficient $D_{ped}(r)$, against the source of electrons from the ionisation of neutral atoms. The neutral densities are modelled in turn by balancing their inward convection with ionisation and charge-exchange sources and sinks. The electron density profile is calculated from the solution of a one-dimensional differential equation for $n_e(x)$ (where $x = r_{rep} - r$, is the radial distance inwards from the separatrix), given by (17) and (18) of Saarelma *et al*. (2023).

The total particle diffusion coefficient in the pedestal region D_{ped} is made up from components due to KBM modes, temperature-gradient-driven ITG and/or ETG driven turbulence (TG) and NC transport, i.e. $D_{ped} = D_{KBM} + D_{TG} + D_{NC}$. Simplified forms for D_{KBM}, D_{TG} and D_{NC} are given by (21)–(26) of Saarelma *et al*. (2023), in which the terms $(D_e/\chi_e)_{TG}$, C_{KBM} and α_{cr} are adjustable parameters of the model. Here, $(D/\chi)_{TG}$ represents the ratio of particle to electron heat flux due to the temperature-gradient driven turbulence and C_{KBM} represents the strength of the KBM turbulence when the normalised pressure-gradient threshold α_{cr} is exceeded.

Boundary conditions are also required to solve the one-dimensional differential equation for $n_e(x)$. The separatrix density $n_{e,sep}$ can be taken from the experiment by finding n_e at the same location as the specified $T_{e,sep}$. Here we take the value $T_{e,sep} = 100\,\mathrm{eV}$, but this can also be calculated using the 2-point model (Stangeby 2000; Kallenbach *et al*. 2005).

The density gradient at the separatrix is set to $dn_e/dx|_{x=0} = -n_e/\sqrt{D_{SOL}\tau_{i,\parallel}}$, where the particle diffusion coefficient D_{SOL}, is calculated from (19) of Saarelma *et al*. (2023) at the separatrix and $\tau_{i,\parallel}$ is thermal ion free-streaming time along the field lines to the divertor. Finally, the FSA neutral particle density $\langle n_{FC}(0)\rangle$ and the ratio of Franck–Condon to charge-exchange particle densities at the separatrix $(n_{FC}/n_{CX})|_{x=0}$ have to be specified.

Tested against a pedestal database of JET-ILW Type I ELMy H-modes (Saarelma *et al*. 2023), this model gave good agreement over a wide parameter range, when using the experimental T_e profile as an input. Further tests for ASDEX Upgrade and MAST-U Type I ELMy H-modes also gave good agreement (Saarelma *et al*. 2024), using the same model parameters used for JET-ILW.

Saarelma *et al*. (2024), further JET-ILW experiments, in which A_{eff} was varied at constant gas rate and constant β_N (Frassinetti *et al*. 2023), could be modelled successfully, provided the experimental variation of $n_{e,sep}$ and the isotope dependence of $(D_e/\chi_e)_{TG}$ were assumed. Over the range $A_{eff} = 2 \rightarrow 3$, appropriate values of $(D_e/\chi_e)_{TG}$ of $0.5 \rightarrow 0.25$ were found from GK simulations Predebon *et al*. (2023), i.e. the relative level of particle to heat transport decreases with increasing A_{eff}.

Appendix C. Sensitivities of the combined ETG+DP model (M3) to input parameters

A comprehensive calculation of the uncertainties on the predicted profiles from the combined ETG+DP+EPED model (M3) using estimated uncertainties on the experimental input parameters is beyond the scope of the present study. However, statements can be made as to how sensitive the predicted $n_{e,ped}$ from the DP model and $T_{e,ped}$ from the ETG model are to the experimental input and internal 'model' parameters of each.

In the discussion below, the sensitivities to the input and model parameters are quantified by assuming a dependence of the calculated parameter y (either $n_{e,ped}$ for the DP model or $T_{e,ped}$ for the ETG model) on the input parameter x as either a power law $y = ax^{\gamma}$ or an offset-linear scaling $y = ax + c$, as appropriate. This allows the sensitivity to be quantified in terms of either the exponent $\gamma = (\Delta y/\Delta x)/(\bar{x}/\bar{y})$, where for example Δx and $\bar{x}$ are the changes and mean values over the scan of the parameter x, or the equivalent, dimensionless coefficient $\gamma = a/(\bar{x}/\bar{y})$ for the offset-linear scaling.

(a) DP model for n_e profile:

(i) Experimental input parameters:

The experimental inputs to this model are: the electron density $n_{e,sep}$ at the separatrix and the heat flux across the separatrix P_{sep}/S. As shown in figure 6 of Saarelma *et al*. (2023), the dependence of $n_{e,ped}$ on $n_{e,sep}$ is slightly weaker than linear, with an estimated scaling exponent $\gamma \sim 0.9$.

The dependence on the heat flux P_{sep}/S across the pedestal, which increases the particle flux in proportion to $(P_{sep}/S)(D/\chi)_{TG}$ and hence decreases $n_{e,ped}$ for increasing P_{sep}, is modest and offset-linear. For example, for JET-Be/W pulse no. 100183, increasing P_{sep} from $8 - 24$ MW decreases $n_{e,ped}$ by only $\sim$12 % from $5.2 \rightarrow 4.6 \times 10^{19}$ m^{-3}, so the scaling coefficient $\gamma \sim 0.12$.

(ii) 'Model' parameters:

The other, less accurately known 'model' parameters of the DP model, to which the $n_{e,ped}$ predictions are mostly less sensitive are: the FSA density of Franck–Condon neutral atoms at the separatrix $\langle n_{FC}(0)\rangle$; the assumed ratio of electron particle diffusivity to electron heat conductivity $(D_e/\chi_e)_{TG}$ across the pedestal; and the ratio of charge-exchange to Franck–Condon neutral densities at the separatrix $(n_{CX}/n_{FC})|_{x=0}$.

As shown in figure 7 of Saarelma *et al*. (2023), the dependence of $n_{e,ped}$ on the neutral density $\langle n_{FC}(0)\rangle$ is modest, with an offset-linear dependence. Increasing $\langle n_{FC}(0)\rangle$ from $0 \rightarrow 10^{16}$ m^{-3} increases $n_{e,ped}$ by $\sim$35 % from $6 \rightarrow 8.5 \times 10^{19}$ m^{-3}, so the scaling coefficient $\gamma \sim 0.17$.

The sensitivity of the $n_{e,ped}$ prediction to the ratio of charge-exchange to Franck–Condon neutral densities at the separatrix is very weak. Calculations performed for JET-Be/W pulse no. 100183, increasing $(n_{CX}/n_{FC})|_{x=0}$ from $0 \rightarrow 0.2$, decreased $n_{e,ped}$ by only $\sim$2.5 %, so the scaling coefficient $\gamma \sim -0.01$.

Increasing the ratio of particle to heat diffusivity $(D_e/\chi_e)_{TG}$ has the same effect as increasing P_{sep}/S, i.e. weakly decreasing $n_{e,ped}$. For example, for pulse no. 96201, doubling $(D_e/\chi_e)_{TG}$ from $0.25 \rightarrow 0.5$ decreased $n_{e,ped}$ by $\sim$12 % from $4.5 \rightarrow 4.0 \times 10^{19}$ m^{-3}, so the scaling coefficient $\gamma \sim -0.2$.

(b) ETG critical-heat-flux model for T_e profile:

(i) Experimental input parameters:

For the ETG critical-heat-flux model, the experimental input parameters are: the heat flux across the separatrix P_{sep}/S and the electron density $n_{e,sep}$ and temperature $T_{e,sep}$ at the separatrix.

The strongest dependencies of $T_{e,ped}$ are on $T_{e,sep}$ and the pedestal–separatrix density ratio $n_{e,ped}/n_{e,sep}$, which can be understood from the simple model for infinitely stiff electron heat transport discussed in § 5.2 above. Assuming that ETG heat transport clamps η_e at some constant level $\bar{\eta}_e$, which is $\mathcal{O}(1)$ above the linear threshold $\eta_{e,cr} \sim \mathcal{O}(1)$, integrating inwards from the separatrix yields relation (5.1), i.e. that T_e at some location x between the separatrix and the density pedestal top is given by $T_e(x) = T_{e,sep}(n_e(x)/n_{e,sep})^{\bar{\eta}_e}$. Hence, for this simple model, $T_{e,ped}$ scales linearly with $T_{e,sep}$ and inversely with $n_{e,sep}^{\bar{\eta}_e}$, where $\bar{\eta}_e \sim \mathcal{O}(2)$ is appropriate for the steep-density gradient region of the pedestal.

Numerical calculations with the full ETG critical-heat-flux model, varying $T_{e,sep}$ at a fixed location on the experimental profiles and hence fixed $n_{e,sep}$ show that T_e at the location of the experimental T_e pedestal location varies approximately linearly with $T_{e,sep}$ as: $T_e(\psi_N^{T_{e,top}}) \approx \mathcal{A}T_{e,sep} + \mathcal{B}$, where the coefficient $\mathcal{A} \sim \mathcal{O}(2)$ increases modestly with the heat flux P_{sep}/S and is typically smaller than that expected from the simple model discussed above, e.g. for JET-Be/W pulse no. 90339, $(n_{e,ped}/n_{e,sep})^{\bar{\eta}_e} \sim 4$ rather than $\sim$2.8, as determined from the $T_{e,sep}$ scan. The offset $\mathcal{B}$, which is typically $\mathcal{O}(\text{few} \times 100\,\text{eV})$, increases weakly with P_{sep}/S and decreases with increasing stiffness of the ETG heat-flux scaling, i.e. with increasing exponent β in (2.1).

(ii) 'Model' parameters:

Sensitivity to the parameters (α, β and $\eta_{e,cr}$) of the gyro-Bohm normalised electron heat-flux scaling (2.1) underlying the model are discussed in Appendix D.1 of Turica *et al*. (2025), which presents a detailed investigation of reconstructions of JET-Be/W T_e profiles from the EUROfusion Pedestal Database (Frassinetti *et al*. 2021), using various reduced turbulence models and machine learning approaches.

In summary of the results in Appendix D.1 of Turica *et al*. (2025):

(i) The strongest dependence of $T_{e,ped}$ is on the critical threshold $\eta_{e,cr}$, increasing $\eta_{e,cr}$ strongly increasing T_e across the pedestal;

(ii) Increasing the coefficient α is equivalent to decreasing the heat flux P_{sep}/S across the pedestal, as the relevant parameter in (2.2) is $P_{sep}/(\alpha S)$. Increasing P_{sep}/S (or decreasing α) only weakly increases $T_{e,ped}$, with an exponent $\gamma \sim \mathcal{O}(0.1)$.

(iii) The stiffness coefficient β affects the shape of the T_e profile but only weakly affects its magnitude. Increased stiffness forces η_e to be closer to the assumed $\eta_{e,cr}$ but it remains larger, so that the term $(\eta_e - \eta_{e,cr})$ in (2.1) remains $\sim\mathcal{O}(1)$, such that the predicted heat flux $q_e \propto (\eta_e - \eta_{e,cr})^{\beta}$ can match the prescribed $q_e = P_{sep}/S$ even when β is very large.

Appendix D. Scaling of upstream density n_u for a collisionless, sheath-limited SOL

For a collisionless, isothermal SOL, assuming that $T_i = T_e$, we have for the temperature $T_u = T_t$ and density $n_u = 2n_t$, where the subscripts u and t denote upstream (mid-plane) and target values respectively (Stangeby 2000). Also assuming a constant SOL power decay length λ_q implies that the parallel electron heat flux in the SOL is proportional to the loss power across the separatrix $q_{\parallel} \propto P_{sep}/S\lambda_q$, where S is the area of the LCFS.

Expressions for the particle and heat fluxes at the target are then: $\Gamma = 1/2 n_t c_s \propto n_t T_t^{1/2}/A^{1/2}$ and $q = \gamma T_t \Gamma \propto n_t T_t^{3/2}/A^{1/2}$, where c_s is the sound speed and $\gamma \sim 5/2$ is the sheath transmission factor. By elimination of n_t from these two expressions, we have $T_t \propto q/\Gamma$, which can be substituted into the expression for Γ to yield the following scaling for the upstream density $n_u \propto \Gamma^{3/2} A^{1/2}/q^{1/2}$.

Hence, even this simple-as-possible model predicts that $n_u \equiv n_{e,sep}$ should increase with isotope mass $\propto A_{eff}^{1/2}$ and also with the particle fuelling rate into the SOL $\propto \Gamma_e^{3/2}$ and decrease with the loss power across the separatrix $\propto P_{sep}^{-1/2}$.

REFERENCES

Adkins, T., Abel, I., Barnes, M., Buller, S., Dorland, W., Ivanov, P., Meyrand, R., Parra, F., Schekochihin, A. & Squire, J. 2026 Asymptotic scaling theory of electrostatic turbulent transport in magnetised fusion plasmas. arXiv preprint arXiv: 2601.15391.

Adkins, T., Schekochihin, A., Ivanov, P. & Roach, C. 2022 Electromagnetic instabilities and plasma turbulence driven by electron-temperature gradient. *J. Plasma Phys.* **88**, 905880410.

Barnes, M., Parra, F. & Schekochihin, A. 2011 Critically balanced ion temperature gradient turbulence in fusion plasmas. *Phys. Rev. Lett.* **107**, 115003.

Candy, J., Belli, E.A. & Bravenec, R. 2016 A high-accuracy eulerian gyrokinetic solver for collisional plasmas. *J. Comput. Phys.* **324**, 73–93.

Chapman-Oplopoiou, B. *et al.* 2022 The role of ETG modes in JET–ILW pedestals with varying levels of power and fuelling. *Nucl. Fusion* **62**, 086028.

Chapman-Oplopoiou, B., Walker, J., Hatch, D.R., Görler, T. & Contributors, J. 2025 Composition of electron temperature gradient driven plasma turbulence in JET-ILW tokamak plasmas. *Phys. Rev. Res.* **7**, L012004.

Dimits, A.M. *et al.* 2000 Comparisons and physics basis of tokamak transport models and turbulence simulations. *Phys. Plasmas* **7**, 969–983.

Federici, G. *et al.* 2014 Overview of eu demo design and r&d activities. *Fusion Engng Des.* **89**, 882–889.

Field, A. *et al.* 2020 The dependence of exhaust power components on edge gradients in JET-C and JET-ILW h-mode plasmas. *Plasma Phys. Control. Fusion* **62**, 055010.

Field, A.R., Chapman-Oplopoiou, B., Connor, J.W., Frassinetti, L., Hatch, D.R., Roach, C.M., Saarelma, S., JET contributors 2023 Comparing pedestal structure in JET-ILW H-mode plasmas with a model for stiff ETG turbulent heat transport. *Phil. Trans. R. Soc. A* **381**, 20210228.

Frassinetti, L. *et al.* 2012 Spatial resolution of the jet thomson scattering system. *Rev. Sci. Instrum.* **83**, 013506.

Frassinetti, L. *et al.* 2016 Global and pedestal confinement and pedestal structure in dimensionless collisionality scans of low-triangularity H-mode plasmas in JET-ILW. *Nucl. Fusion* **57**, 016012.

Frassinetti, L. *et al.* 2019 Role of the pedestal position on the pedestal performance in AUG, JET-ILW and TCV and implications for ITER. *Nucl. Fusion* **59**, 076038.

Frassinetti, L. *et al.* 2021 Role of the separatrix density in the pedestal performance in deuterium low triangularity JET-ILW plasmas and comparison with JET-C. *Nucl. Fusion* **61**, 126054.

Frassinetti, L. *et al.* 2023 Effect of the isotope mass on pedestal structure, transport and stability in D, D/T and T plasmas at similar β_N and gas rate in JET-ILW type I ELMy H-modes. *Nucl. Fusion* **63**, 112009.

Giroud, C. *et al.* 2013 Impact of nitrogen seeding on confinement and power load control of a high-triangularity JET ELMy H-mode plasma with a metal wall. *Nucl. Fusion* **53**, 113025.

Goerler, T., Lapillonne, X., Brunner, S., Dannert, T., Jenko, F., Merz, F. & Told, D. 2011 The global version of the gyrokinetic turbulence code GENE. *J. Comput. Phys.* **230**, 7053–7071.

Groebner, R. *et al.* 2001 Progress in quantifying the edge physics of the H mode regime in DIII-D. *Nucl. Fusion* **41**, 1789.

Groebner, R., Mahdavi, M., Leonard, A., Osborne, T., Porter, G., Colchin, R. & Owen, L. 2002 The role of neutrals in high-mode (H-mode) pedestal formation. *Phys. Plasmas* **9**, 2134–2140.

GROEBNER, R., MAHDAVI, M., LEONARD, A., OSBORNE, T., WOLF, N., PORTER, G., STANGEBY, P., BROOKS, N., COLCHIN, R. & OWEN, L. 2003 Comparison of H-mode barrier width with a model of neutral penetration length. *Nucl. Fusion* **44**, 204.

GUTTENFELDER, W., GROEBNER, R., CANIK, J., GRIERSON, B., BELLI, E. & CANDY, J. 2021 Testing predictions of electron scale turbulent pedestal transport in two DIII-D ELMy H-modes. *Nucl. Fusion* **61**, 056005.

HASSAN, E., HATCH, D., HALFMOON, M., CURIE, M., KOTCHENREUTHER, M., MAHAJAN, S., MERLO, G., GROEBNER, R., NELSON, A. & DIALLO, A. 2021 Identifying the microtearing modes in the pedestal of DIII-D H-modes using gyrokinetic simulations. *Nucl. Fusion* **62**, 026008.

HATCH, D. *et al.* 2015 Gyrokinetic study of ASDEX Upgrade inter-ELM pedestal profile evolution. *Nucl. Fusion* **55**, 063028.

HATCH, D. *et al.* 2019 Direct gyrokinetic comparison of pedestal transport in JET with carbon and ITER-like walls. *Nucl. Fusion* **59**, 086056.

HATCH, D. *et al.* 2021 Microtearing modes as the source of magnetic fluctuations in the JET pedestal. *Nucl. Fusion* **61**, 036015.

HATCH, D.R. *et al.* 2022 Reduced models for ETG transport in the tokamak pedestal. *Phys. Plasmas* **29**, 062501.

HATCH, D., KOTSCHENREUTHER, M., MAHAJAN, S., VALANJU, P., JENKO, F., TOLD, D., GÖRLER, T. & SAARELMA, S. 2016 Microtearing turbulence limiting the JET-ILW pedestal. *Nucl. Fusion* **56**, 104003.

HATCH, D., KOTSCHENREUTHER, M., MAHAJAN, S., VALANJU, P. & LIU, X. 2017 A gyrokinetic perspective on the JET-ILW pedestal. *Nucl. Fusion* **57**, 036020.

HORTON, L. *et al.* 2005 Characterization of the H-mode edge barrier at ASDEX Upgrade. *Nucl. Fusion* **45**, 856.

HOWARD, N., HOLLAND, C., WHITE, A., GREENWALD, M. & CANDY, J. 2015 Multi-scale gyrokinetic simulation of tokamak plasmas: enhanced heat loss due to cross-scale coupling of plasma turbulence. *Nucl. Fusion* **56**, 014004.

IKEDA, K. 2009 Iter on the road to fusion energy. *Nucl. Fusion* **50**, 014002.

JENKO, F. 2000 Massively parallel Vlasov simulation of electromagnetic drift-wave turbulence. *Comput. Phys. Commun.* **125**, 196–209.

JENKO, F., DORLAND, W. & HAMMETT, G. 2001 Critical gradient formula for toroidal electron temperature gradient modes. *Phys. Plasmas* **8**, 4096–4104.

JENKO, F., TOLD, D., XANTHOPOULOS, P., MERZ, F. & HORTON, L. 2009 Gyrokinetic turbulence under near-separatrix or nonaxisymmetric conditions. *Phys. Plasmas* **16**, 055901.

KALLENBACH, A., ASAKURA, N., KIRK, A., KOROTKOV, A., MAHDAVI, M., MOSSESSIAN, D. & PORTER, G. 2005 Multi-machine comparisons of h-mode separatrix densities and edge profile behaviour in the itpa sol and divertor physics topical group. *J. Nucl. Mater.* **337–339**, 381–385, pSI-16.

KOTSCHENREUTHER, M. *et al.* 2019 Gyrokinetic analysis and simulation of pedestals to identify the culprits for energy losses using 'fingerprints'. *Nucl. Fusion* **59**, 096001.

LEPPIN, L. *et al.* 2023 Complex structure of turbulence across the ASDEX Upgrade pedestal. *J. Plasma Phys.* **89**, 905890605.

MAGGI, C. *et al.* 2015 Pedestal confinement and stability in JET-ILW ELMy H-modes. *Nucl. Fusion* **55**, 113031.

MAGGI, C. *et al.* 2017 Studies of the pedestal structure and inter-ELM pedestal evolution in JET with the ITER-like wall. *Nucl. Fusion* **57**, 116012.

MIKHAILOVSKII, A., HUYSMANS, G.T., KERNER, W.O. & SHARAPOV, S. 1997 Optimization of computational MHD normal-mode analysis for tokamaks. *Plasma Phys. Rep.* **23**, 844–857.

NEUHAUSER, J. *et al.* 2002 Transport into and across the scrape-off layer in the ASDEX Upgrade divertor tokamak. *Plasma Phys. Control. Fusion* **44**, 855.

NUTTALL, W.J., KONISHI, S., TAKEDA, S. & WEBBE-WOOD, D. 2020 *Commercialising Fusion Energy*. IOP Publishing Limited.

PARISI, J.F. *et al.* 2020 Toroidal and slab ETG instability dominance in the linear spectrum of JET-ILW pedestals. *Nucl. Fusion* **60**, 126045.

Pasqualotto, R., Nielsen, P., Gowers, C., Beurskens, M., Kempenaars, M., Carlstrom, T., Johnson, D., JET-EFDA Contributors 2004 High resolution Thomson scattering for Joint European Torus (JET). *Rev. Sci. Instrum.* **75**, 3891–3893.

Predebon, I., Hatch, D., Frassinetti, L., Horvath, L., Saarelma, S., Chapman-Oplopoiou, B., Görler, T., Maggi, C. & Contributors, J. 2023 Isotope mass dependence of pedestal transport in JET H-mode plasmas. *Nucl. Fusion* **63**, 036010.

Pueschel, M., Hatch, D., Ernst, D., Guttenfelder, W., Terry, P., Citrin, J. & Connor, J. 2019 On microinstabilities and turbulence in steep-gradient regions of fusion devices. *Plasma Phys. Control. Fusion* **61**, 034002.

Pueschel, M., Hatch, D., Kotschenreuther, M., Ishizawa, A. & Merlo, G. 2020 Multi-scale interactions of microtearing turbulence in the tokamak pedestal. *Nucl. Fusion* **60**, 124005.

Reiter, D., May, C., Coster, D. & Schneider, R. 1995 Time dependent neutral gas transport in tokamak edge plasmas. *J. Nucl. Mater.* **220**, 987–992.

Romanelli, F. 1989 Ion temperature-gradient-driven modes and anomalous ion transport in tokamaks. *Phys. Fluids B: Plasma Phys.* **1**, 1018–1025.

Réfy, D.I., Brix, M., Gomes, R., Tál, B., Zoletnik, S., Dunai, D., Kocsis, G., Kálvin, S., Szabolics, T., JET Contributors 2018 Sub-millisecond electron density profile measurement at the JET tokamak with the fast lithium beam emission spectroscopy system. *Rev. Sci. Instrum.* **89**.

Saarelma, S. *et al.* 2024 Density pedestal prediction model for tokamak plasmas. *Nucl. Fusion* **64**, 076025.

Saarelma, S., Connor, J., Bilkova, P., Bohm, P., Field, A., Frassinetti, L., Fridstrom, R., Kirk, A. & Contributors, J. 2023 Testing a prediction model for the H-mode density pedestal against JET-ILW pedestals. *Nucl. Fusion* **63**, 052002.

Schneider, P.A. *et al.* 2023 Isotope physics of heat and particle transport with tritium in JET-ILW type-I ELMy H-mode plasmas. *Nucl. Fusion* **63**, 112010.

Simpson, J., Moulton, D., Giroud, C., Groth, M., Corrigan, G. & Contributors, J. 2019 Using EDGE2D-EIRENE to simulate the effect of impurity seeding and fueling on the upstream electron separatrix temperature. *Nucl. Mater. Energy* **20**, 100599.

Snyder, P., Groebner, R., Leonard, A., Osborne, T. & Wilson, H. 2009 Development and validation of a predictive model for the pedestal height. *Phys. Plasmas* **16**, 056118.

Snyder, P., Wilson, H., Ferron, J., Lao, L., Leonard, A., Osborne, T., Turnbull, A., Mossessian, D., Murakami, M. & Xu, X. 2002 Edge localized modes and the pedestal: a model based on coupled peeling–ballooning modes. *Phys. Plasmas* **9**, 2037–2043.

Stangeby, P.C. 2000 *The Plasma Boundary of Magnetic Fusion Devices*. CRC Press.

Told, D. *et al.* 2008 Gyrokinetic microinstabilities in asdex upgrade edge plasmas. *Phys. Plasmas* **15**, 102306.

Turica, L.P., Field, A.R., Frassinetti, L., Schekochihin, A.A., Contributors, J. & the EUROfusion Tokamak Exploitation Team 2025 Reconstructions of electron-temperature profiles from eurofusion pedestal database using turbulence models and machine learning. arXiv: 2504.17486.

Wagner, F. *et al.* 1982 Regime of improved confinement and high beta in neutral-beam-heated divertor discharges of the asdex tokamak. *Phys. Rev. Lett.* **49**, 1408–1412.